THESIS FOR THE DEGREE OF DOCTORATE OF PHILOSOPHY
IN NATURAL SCIENCE, SPECIALIZING IN PHYSICS

MULTIPHOTON MICROSCOPY ENHANCED: EXPLORING ANNULAR BEAMS AND GOLD NANOPARTICLES FOR IMPROVED IMAGING

JOHAN BORGLIN

UNIVERSITY OF GOTHENBURG

Department of Chemistry & Molecular Biology
Department of Physics
University of Gothenburg
SE-412 96 Gothenburg Sweden 2016

Multiphoton microscopy enhanced:
Exploring annular beams and gold nanoparticles for improved imaging
JOHAN BORGLIN
ISBN 978-91-628-9787-1 (Print)
ISBN 978-91-628-9786-4 (PDF)
http://hdl.handle.net/2077/42385

Doctoral thesis at University of Gothenburg

Front page:
Upper left: Multi-photon FLIM of human skin stained with RhodaminB and possible mite. See Section 5.3.1
Upper right: Logarithm of simulated focal volume, see Section 5.1.1
Lower left: Clusters of gold nanoparticles in solution exhibiting MIL in a multiphoton microscope. See Section 5.2.3
Lower right: Scattering skin phantom, stained gauze in agar and fluorescin. See Section 5.1.2

Biomedical Photonics Group
Department of Chemistry and Molecular Biology
University of Gothenburg
SE-412 96 Göteborg
Telephone: +46 (0)31 768 0000

Printed by Kompendiet
Gothenburg, Sweden 2016

For Family
For Friends
For Science

Abstract

Laser scanning multiphoton microscopy (MPM) has emerged as a powerful tool for non-invasive three-dimensional imaging of biological tissue. The localized focal region enables confocality without the use of a physical pinhole while providing less photobleaching and photodamage compared to confocal laser scanning microscopy. As imaging depth increases, the capabilities of MPM becomes significantly limited by overwhelming background fluorescence and decreased contrast, particularly within highly light scattering tissue. This thesis presents two routes for improving the signal in MPM, involving beam shaping of the excitation laser, and using functionalized gold-nanoparticles (AuNPs) as contrast media. In addition, an experimental MPM system is presented. This system was set up to conduct proof-of-principle experiments.

Theoretical calculations, performed as part of the project, show that annular laser beams could reduce out-of-focus fluorescence when performing MPM, especially in optically dense media. This novel technique is evaluated both mathematically and experimentally. Computer simulations have been performed to predict the theoretical viability of the technique, and proof-of-principle experimentally performed in tissue phantoms and excised tissue samples have been conducted. Initial results demonstrate that the background signal can be reduced by the use of annular beams, which will lead to an increased imaging depth. Further refinements are required to gain full potential of the approach.

As an additional approach to improving MPM, spherical AuNPs were explored as contrast mediators, through the use of multiphoton induced luminescence (MIL). Investigations of AuNPs deposited on gradient substrates show that particle aggregation is required in order to give rise to a detectable signal in far-field MPM. This insight led to the application of a system of 20 nm AuNPs functionalized with synthetic peptides in solution. Upon addition of Zn^{2+}, the particles aggregate which enables the MIL process. Thus, this system is of interest for future development of a switchable contrast media, which will further enhance the capabilities of MPM.

An experimental MPM developed setup was designed and assembled to implement the annular beams. It will allow exploration of fluorescence life-time imaging and multiphoton induced photodynamic effects in a systematic manner. Initial data from the experimental platform are presented. This thesis comprehensively demonstrates the potential of improving and expanding the possibilities for MPM in biomedical research.

Keywords: Multiphoton microscopy, Annular beams,
Gold nanoparticles, Multiphoton induced luminescence

Research publications

The work presented in this thesis is based upon four research articles, referred to as Paper I - IV.

Paper I

Improving multi-photon microscopy using annular beam shaping, focusing on imaging of human skin
J. Borglin, N. Durr, S. Guldbrand, O. Ferhanoglu, A.-M. Wennberg, D. Hanstorp, A. Ben-Yakar, M. B. Ericson
Proc. SPIE Proc., 8948, 2014

Paper II

Insights on proximity effect and multiphoton induced luminescence from gold nanospheres in far field optical microscopy
J. Borglin, S. Guldbrand, H. Evenbratt, V. Kirejev, H. Grönbeck, M. B. Ericson
Applied Physics Letters, 2015. 107(23): p. 234101.

Paper III

Functionalized gold nanoparticles as switchable contrast medium in multiphoton microscopy
J. Borglin, R. Selegård, D. Aili, M. B. Ericson
To be submitted to Small Communications.

Paper IV

Exploring annular beam shaping to improve imaging depth for multiphoton microscopy in turbid medium
J. Borglin, D. Wang, , M. B. Ericson
To be submitted to Journal of Biomedical Optics.

Contribution report

The contributions by the author (JB) to the appended papers have been the following:

Paper I: JB performed the study based on an idea provided by MBE, ND and ABY, and wrote the manuscript.

Paper II JB provided theoretical insights together with HG and MBE. JB performed additional experiments to those performed by SG and HE. JB wrote the final manuscript together with MBE

Paper III JB performed the MIL experiments and wrote the manuscript. DA developed the particle system and performed the TEM measurements.

Paper IV JB designed and implemented the experimental setup. JB performed the data collection and wrote the manuscript together with DW.

MBE	Marica. B. Ericson
ND	Nicholas Durr
ABY	Adela Ben-Yakar
SG	Stina Guldbrand
HE	Hanne Evenbratt
HG	Henrik Grönbeck
DA	Daniel Aili
DW	Danni Wang

Paper not included in this thesis:

Multi-photon microscopy – a powerful tool in skin research and topical drug delivery science
V. Kirejev, S. Guldbrand, J. Borglin, C. Simonsson, M. B. Ericson
Published in Journal of Drug Delivery Science and Technology, 22, **3**, p250-259 (2012)

Abbreviations

AFM	Atomic force microscopy
AuNPs	Gold nanoparticles
CLSM	Confocal laser-scanning microscopy
FAD	Flavine adenine dinucleotide
FIFO	First-in-first-out memory
FLIM	Fluorescence lifetime imaging
FPGA	Field-programmable gate array
FRET	Förster resonance energy transfer
FCS	Fluorescence correlation spectroscopy
LSPR	Localized surface plasmon resonance
MIL	Multiphoton-induced luminescence
MPM	Multiphoton microscopy
NA	Numerical aperture
NADH	Aicotinamide adenine dinucleotide
NIR	Near-infra-red
PALM	Photo-activated localization microscopy
PMT	Photomultiplier tube
ROI	Region of interest
SEM	Scanning electron microscopy
SLM	Spatial light modulator
STED	Stimulated emission depletion
TEM	Transmission electron microscopy
TCSPC	Time-correlated single-photon counting
UV	Ultraviolet
VI	Virtual instrument

Symbols

α	Maximal half-angle of lens
α_i	Incident angle
α_r	Reflection angle
α_d	Deflection angle
a_0	Aperture exit diameter
b	Inner beam radius at lens
$b´$	Inner beam radius
B	Max beam radius at lens
$B´$	Max beam radius
e	Base of the natural logarithm
f	Focal length
I	Intensity
λ	Wavelength
n	Refractive index
P_0	Power at lens
r	Radial coordinate at lens
$r´$	Radial coordinate
θ	Azimuthal coordinate at lens
$\theta´$	Azimuthal coordinate
t	Time
t_n	Lifetime of n:th fluorophore
$\Psi´$	Field amplitude
$\Psi´_{fk}$	Field amp. calculated from the Fresnell-Kirchhoff integral
z	Sample depth coordinate

Contents

1 Introduction

Microscopy design has evolved from pieces of equipment constructed from two lenses to complex systems comprising of lenses, detectors, computers and sophisticated light sources capable of detecting *e.g.* the fluctuations of single molecules [1, 2]. Recent advances in the optical microscopy field include powerful techniques such as stimulated emission depletion (STED) and photo-activated localization microscopy (PALM), which allow for imaging at resolutions below the diffraction limit [3-6], allowing miniscule objects, *e.g.* individual proteins, to be studied using optical microscopy. The inventors behind these two techniques were awarded with the Nobel Prize in chemistry 2014.

In confocal laser scanning microscopy (CLSM), a laser is used to scan the sample, pixel by pixel, and computers reconstruct the images in 3D. In multiphoton microscopy (MPM), quantum effects that initially could only be derived in theory [7], are utilized for non-invasive tissue imaging, allowing further exploration into the nature of our bodies [8, 9]. Both techniques have been developed for clinical use [10, 11][1], and have shown great potential, not the least within the field of dermatology.

Human skin has been widely recognized as the window to evaluation of pathological processes [12]. Due to its large scattering properties, the skin is considered the most difficult organ to investigate non-invasively beyond superficial depths using optical methods. From the perspective of optical engineering, developing an optical microscope capable of non-invasively visualize and monitor disease progression within the skin is a significant milestone, as the applications will broadly impact the field of biomedical photonics in general. From a pharmacological development perspective, understanding the protective and transport mechanisms of the skin allows for the development of topically delivered drugs utilizing novel transdermal

[1]CLSM: VivaScope (Lucid Inc., Rochester, MN, USA) and MPM: DermaInspect (JenLab GmbH, Neuengönna, Germany)

pathways [13]. From a clinical diagnostics point of view, providing an alternative to the diagnostic procedure of biopsy followed by histopathology for skin cancer diagnostics can potentially revolutionize the diagnostic paradigm [14-23].

MPM has shown great potential for investigations in skin [24-29], allowing for the detection of auto-fluorescence and exogenous contrast media. This allows the visualization of cell structures, as well as the distribution of compounds added to the skin [30]. By tuning the excitation wavelength to the absorption band of a specific fluorophore, selectivity can be achieved. MPM uses near-infrared (NIR) light which penetrates the skin more efficiently than the visible light commonly used in CLSM [31]. Commonly, the imaging depth is limited by the scattering components within the tissue. The imaging depth can be extended by increasing the power of the excitation laser. However, photo-damage and out-of-focus fluorescence scale with laser power, putting a limit to the imaging depth in conventional MPM [32]. Another approach is to use contrast agents with bright fluorescence.

Gold nanoparticles (AuNPs), which have been explored within the biological research field for more than a decade [33-35], have recently gained interest as a contrast agent in MPM. AuNPs carry remarkably different properties from gold in bulk state, which is easily visible from the color. A solution of AuNPs ("colloidal gold") can vary in color from pale pink to deep red [36] while gold in bulk state has a yellowish color. In MPM, they can be visualized based on their ability to exhibit multiphoton induced luminescence (MIL) [37, 38], a process still not fully understood. Research shows that AuNPs are capable of entering human cells, but are not acutely cytotoxic, which allows them to be used to enhance the imaging of human tissue [39].

This thesis presents the development of a novel MPM platform utilizing knowledge from optical engineering and physical chemistry. We explored how to visualize deeper into biological specimens by modifying the illumination laser beam into an annular beam. Annular beams have previously been explored for increased image resolution [40-42], while the technique, within the scope of this thesis, was explored as a means to reject out-of-focus fluorescence in optically dense media. In addition, it was concluded that the luminescence of

AuNPs can be controlled by controlling the inter-particle distance, and thus creating a switchable contrast media, capable of further enhance imaging in biological samples.

2 Background

This chapter aims to provide an introduction to optical microscopy in general, and laser scanning microscopy in particular. As CLSM and MPM are deeply connected, background is provided for both. In addition, a general overview of a MPM microscope is provided. Fluorescence lifetime imaging (FLIM), an extension of laser scanning microscopy, is described in detail, as the technique is implemented on the experimental MPM setup. In addition, gold nanoparticles and their role in enhancing contrast for microscopy is explained.

2.1 Light and microscopy

Light has been used in imaginative ways since ancient times. Transparent polished crystals has been used to optically magnify objects and to focus sunlight to create fire as early as in ancient Greece [43]. However, optical microscopy as we know it did not exist until the 16th century, when the field was pioneered by people such as the Janssen brothers, Galileo, Hooke and van Leeuwenhoek [44, 45]. As suggested by the name (from Greek words for “small” and “to view”), in the field of microscopy, light is used to view things too small for the bare human eye to resolve. The first microscopes used lenses to gather the light reflected off, or transmitted through, a large part of the sample. This kind of microscope is still widely used today. Further progress was made with the invention of the wide-field fluorescence microscopy. This technique uses light to excite fluorescent molecules (fluorophores) in the sample, which in turn provide signal for image formation.

With the invention of the laser in the 1960’s, scientists had access to a source of coherent light with a low bandwidth [46]. This sparked several new inventions, such as fiber-optic signal transmission and surveying tools, and lasers are found in all parts of our daily lives today. However, it would take until 1986 before a fully functioning laser scanning microscope was developed [47-49].

2.2 Confocal microscopy

Confocal laser scanning microscopy was developed to improve upon widefield fluorescence microscopy, where the out-of-focus fluorescence severely degraded the imaging quality. [50] A comparison is shown in Figure 2.1, where the same cell is imaged using both widefield and confocal fluorescence microscopy. As CLSM allows optical sectioning, it also enabled the collection of three-dimensional data-sets. Due to the inherent confocality of the technique, the out-of-focus signal is normally not present in MPM, but shows up at high laser powers. Annular beams, explored in this thesis, provide a possible way around this problem. A generalized confocal setup is shown in Figure 2.2.

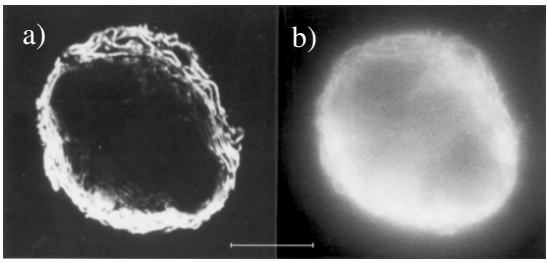

Figure 2.1. A comparison between a), an image acquired using confocal laser scanning microscopy and b), one acquired with wide-field fluorescence microscopy. The sample imaged is a plasmacytoma cell labelled with anti-endoplasmin, which binds chiefly to cisternae of the endoplasmic reticulum. As the wide-field fluorescence image is constructed from fluorescence signal from the entire cell, a high out-of-focus signal is visible. This signal is spatially filtered out in CLSM. Scale bar = 10 um [47, 48]. Reprinted with permission from [48].

In confocal microscopy, the laser beam is scanned across the sample, usually using mirrors. The generated fluorescence is detected and correlated to a pixel through the position of the mirrors. After the focus of the laser is moved, the signal measured from a new point is translated to the intensity of a new pixel. A confocal pinhole is used to reject out-of-focus fluorescence and ensure that the measured signal originates from the focal plane. The focus of the laser is moved over a range of depths within the sample to acquire a 3D stack of images [51]. The resulting 3D data-matrix allows the volume to be visualized in the computer as slices along the spatial dimensions.

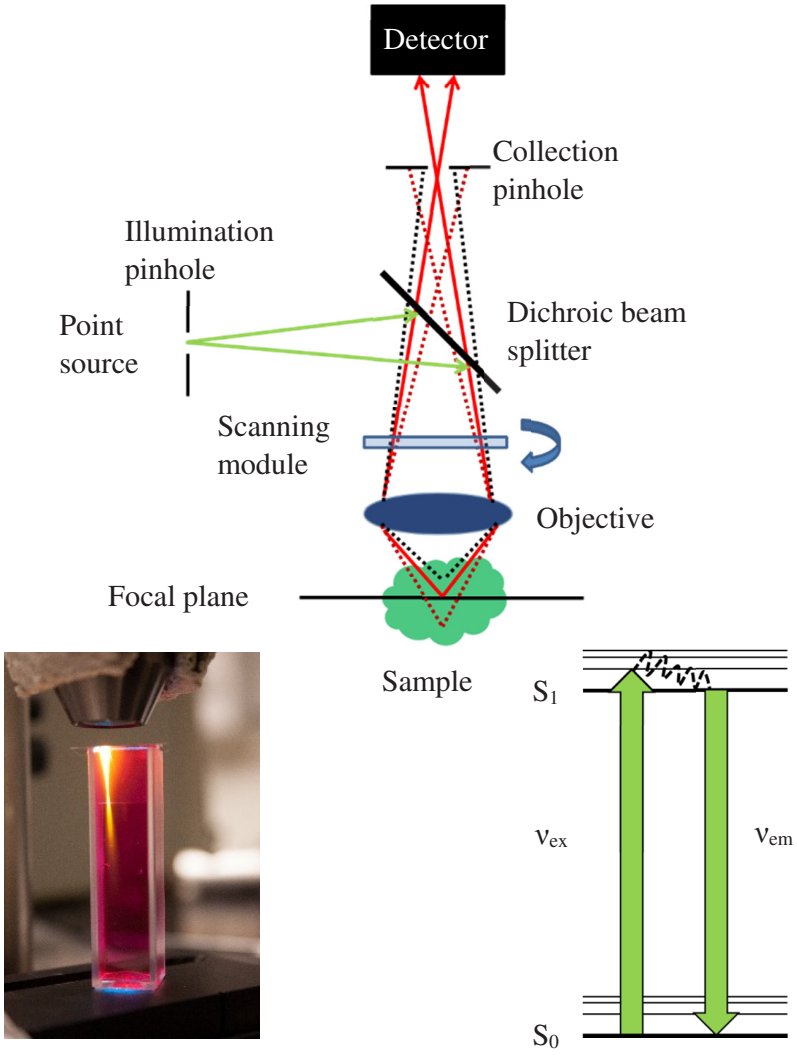

Figure 2.2. The general principle behind confocal microscopy, where a point in the focal plane is imaged at the imaging aperture by utilizing a one-photon process. The signal from a point outside the focal plane is largely rejected by the aperture. The scan module is placed after the dichroic mirror to keep the aperture in focus (descanned detection). Included is also a photo from an Argon laser ($\lambda = 488$ nm) exciting rhodamine-B dissolved in water, through a one-photon process. Finally, a Jablonski diagram which shows the ground state S_0 and the first excited state S_1 of the fluorophore, as well as the excitation photon ν_{ex} and the emitted photon ν_{em}.

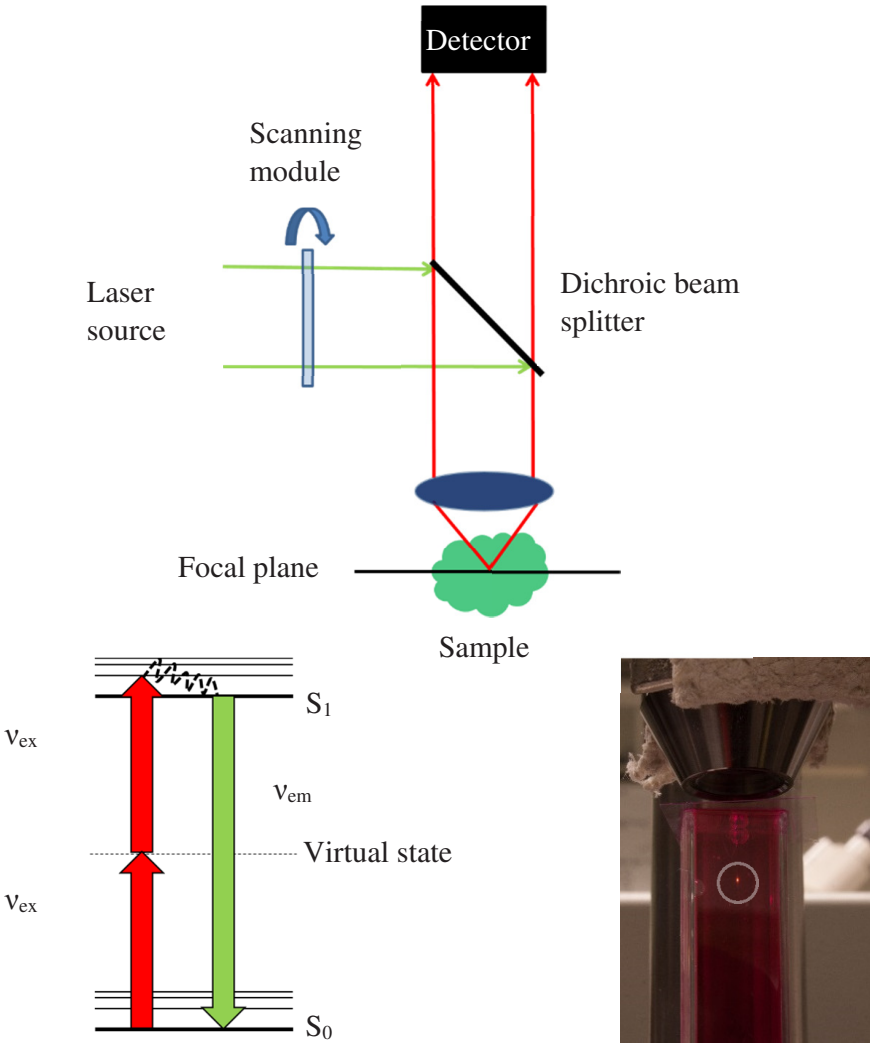

Figure 2.3. The general principle behind MPM. Because of the inherent localization of the multiphoton process, all fluorescence is generated in the focal plane, and no confocal pinhole is needed, which in turns enables the scan module to be placed before the dichroic mirror (non-descanned detection). The image also includes a Jablonski diagram which shows the ground state S_0 and the first excited state S_1 of the fluorophore, as well as the two excitation photons ν_{ex} and the emitted photon ν_{em}. A photo of a Ti-Sapphire laser (λ = 800 nm, pulsed) exciting rhodamine-B dissolved in water is shown. The focal volume is circled.

2.3 Multiphoton microscopy

Much like in CLSM, a laser is used in MPM to excite the fluorophore, but instead of using a pin-hole to filter out out-of-focus fluorescence, the technique utilizes the properties of a multiphoton process [7, 8]. The general principles of a multiphoton process are shown in Figure 2.3. In this process, low-energy photons are used, such that no one-photon excitation of the fluorophore can occur. If the photon flux at one point is high enough, there exists a real probability that the fluorophore will absorb two or more photons almost simultaneously through a virtual state. Since the process requires multiple photons, it will depend non-linearly on the excitation laser power. If the laser power is chosen appropriately, this will only happen at the focus of the optical system. The time window for this process is narrow, and the photons have to be absorbed within 10^{-16} s or shorter. The theory behind the multiphoton absorption was conceived by Maria Göppert Mayer in her PhD thesis in 1930 [7] but could not be actualized until the invention of lasers [8]. In the last decade, the technique has rapidly found its place in the medical sciences [9, 24, 27, 52, 53]. A microscope building upon this process is described in Sections 2.3.2 and 4.3 of this thesis.

Contrast in laser scanning microscopy can either be provided by endogenous (auto-fluorescence) or exogenous fluorophores. The use of endogenous contrast agents comes with the benefit of not having to introduce a foreign substance into the sample. Exogenous contrast agents added to the sample can provide a stronger signal. The agents can be unspecific, like fluorescein, or can be made to specifically bind to and label *i.e.* different cell parts using functionalization with antibodies [54]. When using exogenous contrast agents, the toxicity of the agent must be evaluated, as well as how it affects the system measured. Many metal nanoparticles are used as contrast agents [55]. The ability to selectively visualize components in MPM is important for the development of optical microscopy, and is further explored in Paper III.

2.3.1 Multiphoton microscopy in skin

MPM out-performs CLSM in certain applications, especially when imaging in biological tissue, e.g. skin [56], as the longer wavelengths used to achieve the lower photon energy falls in the "optical window" of biological tissue [57], illustrated in Figure 2.4. In this wavelength band, the tissue is not absorbing as much of the light as it does at other wavelengths. It has been shown that MPM performs better than CLSM in highly scattering biological samples [58].

Skin anomalies can be detected by an increase in metabolic activity of epithelial cells, which in turn affects the emission intensities of the nicotinamide adenine dinucleotide (NADH), and flavine adenine dinucleotide (FAD) coenzymes [59]. However, achieving sufficient signal levels to distinguish the imaged feature from the background might prove to be a challenge.

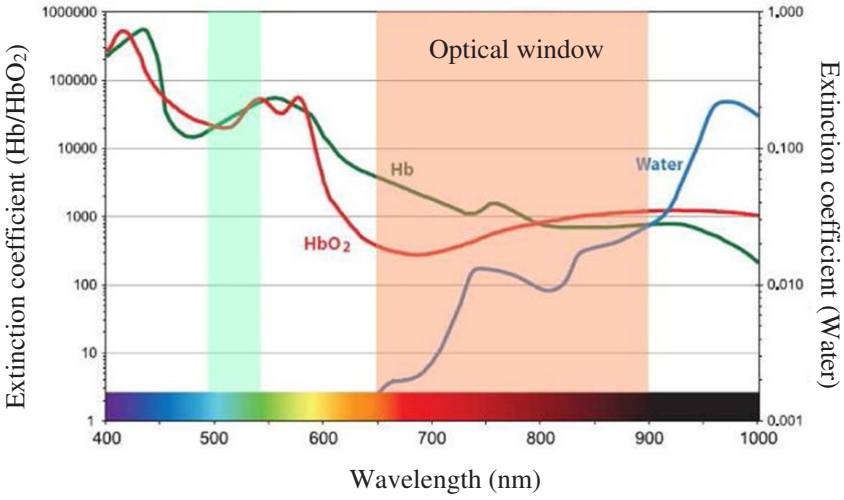

Figure 2.4. Graphs showing the logarithm of the absorption of oxyhemoglobin (HbO_2), hemoglobin (Hb), and water, all of which are major absorbers in skin. In the "optical window" (red), the combined absorption of these components is minimal [60, 61]. Used with permission (CC BY 3.0).

Other applications of MPM in skin include collagen imaging, using second harmonic generation (SHG) [62], and detection of protoporphyrin IX in non-melanoma skin cancer [63].

2.3.2 A multiphoton microscope

This section describes a general MPM setup from the laser, through the optical path and into the sample. An example of such a setup is shown in Figure 2.5. The concepts of focal volumes and out-of-focus fluorescence will be discussed, as well as the detectors and data collection hardware and the software responsible for collecting data and controlling the microscope.

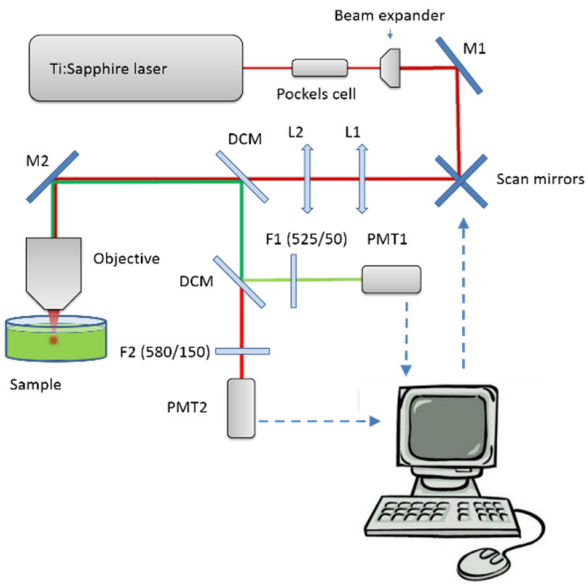

Figure 2.5. A typical MPM setup compromised of a pulsed laser, a Pockels cell for intensity modulation, a beam expander and scan mirrors to scan the beam across the sample. The laser is focused with an objective, which also leads the signal back to the detectors (PMTs). The setup include mirrors (M1-2), lenses (L1-2), dichroic mirrors (DCM) and filters (F1-2). A Pockels cell provides a way to modulate the intensity of the laser through an applied voltage.

2.3.2.1 Optical path

In order to generate the high photon flux needed to achieve a detectable multiphoton signal, a pulsed laser is essential (for biomedical purposes). The short pulses (typically with a pulse-length of ~100 fs) make sure that while the laser can deliver a high peak power, the average power is kept low. A higher average laser power would lead to damage of the sample, both from increased photo-damage and from burning [64], while a lower peak power would mean that not enough photons arrive at the focal volume at the same time to achieve a detectable signal [8]. Commonly, a Ti:Sapphire laser is used as an excitation source.

Scanning is achieved by a pair of galvo mirrors controlled by the data acquisition software. The scan mirrors are imaged through a pair of lenses (L1-2 in Figure 2.5) to the back aperture of the objective. The position of the lenses can be calculated using the equations presented by Tsai *et al.* [65] to ensure a stationary pivoting point for the beam at the back aperture of the objective, as illustrated in Figure 2.6. The different distances are calculated using the equations

$$d_2 = f_1 + f_2 \tag{1}$$

and

$$d_1 = \frac{(f_1)^2}{f_2} + f_1 - d_3\left(\frac{f_1}{f_2}\right)^2. \tag{2}$$

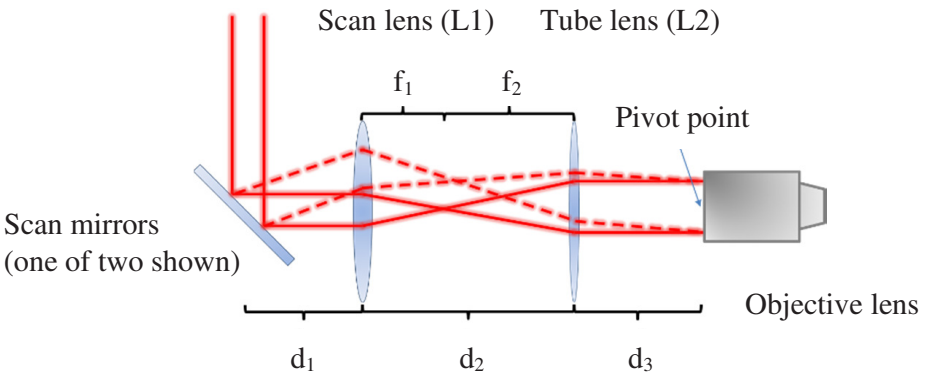

Figure 2.6. The laser scanning system consisting of a pair (only one shown) of galvo mirrors, a scanning lens (L1 in Figure 2.5), a tube lens (L2 in Figure 2.5), and the objective. The dashed lines show the outline of a laser beam diverted away from the center of the first lens to achieve scanning.

The mirrors are close enough to each other to be considered co-localized for the purposes of these calculations.

A microscope objective is used for focusing the beam into the sample, which creates the high photon density needed for a detectable signal to be generated. An objective with high numerical aperture (NA) is preferred, to obtain a confined focal volume and maximize the collection efficiency. NA is illustrated in Figure 2.7a. The NA of an objective is a number which describes the relation between the focal distance *f*, the diameter *D* of the objective, and *n*, the refractive index of the immersion media. NA is defined as

$$NA = n \sin \alpha \approx n \frac{D}{2f}, \tag{3}$$

where α is the angle between the optical axis and the ray hitting the edge of the objective exit aperture, calculated as

$$\alpha = \tan^{-1} \frac{D}{2f}. \tag{4}$$

n is proportional to the NA. Therefore, a water-immersed objective has a higher NA than a dry objective with the same diameter and working distance.

2.3.2.2 Focal volume and point spread function

The exciting light is focused by the microscope objective. Due to the wave-nature of light, the focus of the light can never be a point, but rather a volume, referred to as the focal volume. A system with a minimal focal volume is called a diffraction limited system. The shape of the focal volume, and therefore the optical resolution, is described by the intensity point spread function (IPSF). The IPSF for a focused Gaussian beam can be calculated by fitting Gaussian functions to the height and width of the intensity profiles. The *1/e* radii for *x/y* and *z* (see Figure 2.7b) can then be obtained [24, 66] with the equations

$$\omega_{xy} = \begin{cases} \dfrac{0.320\lambda}{\sqrt{2}\mathrm{NA}} & \mathrm{NA} \leq 0.7 \\ \dfrac{0.325\lambda}{\sqrt{2}\mathrm{NA}^{0.91}} & \mathrm{NA} > 0.7 \end{cases} \tag{5}$$

and

$$\omega_z = \frac{0.532\lambda}{\sqrt{2}}\left[\frac{1}{n - \sqrt{n^2 - \mathrm{NA}^2}}\right]. \tag{6}$$

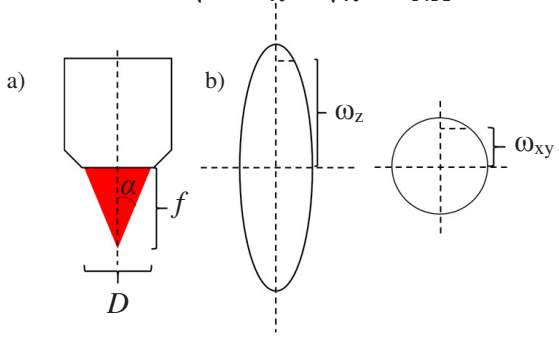

Figure 2.7. Schematic illustrations of a) the focal volume, and b) the concept of NA

2.3.2.3 Out-of-focus fluorescence in MPM

The main feature of MPM is, as previously noted, that the signal is only generated in the focal volume. It has been shown by Durr *et al.* [32]. However, that this only holds true up to a certain intensity of the excitation laser, especially in highly scattering biological samples. This effect is schematically illustrated in Figure 2.8. When the intensity exceeds this threshold, fluorescence is generated outside of the focus of the laser, starting at the sample surface. This fluorescence will degrade the image quality and eventually over-shadow the desired signal [32, 67]. In this thesis, this problem is addressed through the use of annular beams, further described in 3.1.

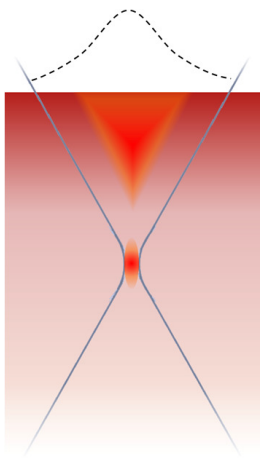

Figure 2.8. A schematic illustration of the out-of-focus fluorescence, which is generated at the surface of the sample when the laser intensity reaches a high level.

2.3.2.4 Data collection

The signal photons generated by the multiphoton process in the sample is emitted from the laser focus in a random direction. While most of the signal will be scattered and/or absorbed by the sample, some of the generated photons will travel back through the objective. As the energy of the emitted photons has almost doubled, they can be

deflected by a dichroic mirror to the detectors. Only the photons reaching the detector can contribute to the result of the measurement, and care must be taken to align the detectors with the sample.

The detectors, often photo-multiplier tubes (PMTs), detect the incoming signal, and converts it to an electric current, which in turn is read by some kind of hardware, described in the following text. There are several ways to read out the detectors. The two ways described here were both used in the experimental setup described later.

The first approach involves reading the accumulated charge from the PMTs. A pre-amplifier converts the initial current from the PMTs to a voltage, which is read by a voltage meter connected to data collection hardware, *i.e.* a field-programmable gate array (FPGA) [68]. The signal measured is proportional to the number of photons detected during a short time interval, and can be used to create an intensity image. While not the only alternative, the FPGA provides a reliable clock, which is used to synchronize the different hardware elements with the software, and which makes sure all pixels correspond to equal exposure times.

In the second approach, time-correlated single photon counting (TCSPC) can be implemented to count the current bursts generated by individual photons [69]. This allowed for a time-resolved data collection. For every photon collected, a timestamp is stored, and correlated with the time since the last laser pulse. Using TCSPC allows for detection of fluorescent lifetimes, a technique described in 2.5.

While the TCSPC approach provides time-resolution, the FPGA approach could provide a higher photon count, since the currents generated by the photons builds up a charge, which is read out at one time. In the TCSPC approach, the detectors are read out continuously, and a maximum of one photon per pulse can be detected.

2.4 Laser beam modulation and spatial light modulators

Many applications require modulation of the excitation laser beam. The equipment used and the complexity of the modulation vary greatly, from a basic shutter to the far more complex spatial light modulator (SLM). Four different types of modulators are used in the microscopy setup presented in this thesis. All, except the shutter, are described here.

An acousto-optic modulator uses sound (pressure) waves to change the optical properties of a material. In ultra-fast lasers, this effect is used in the laser cavity to reflect the beam off a moving surface. This causes a Doppler-shift in the beam, which helps achieve pulsing of the laser ("mode-locking") where the laser outputs short bursts of energy with extremely high peak intensity [70].

A Pockels cell is another type of beam modulator. Here, the electro-optical effect is used to modulate the beam. A voltage is applied over a potassium, hydrogen, and phosphorus crystal, which turns the polarization of the beam as a function of the applied voltage. When combined with a polarizer, this can be used to modulate the intensity of the beam [71].

The term spatial light modulator is a general term which refers to devices which can modulate the phase, polarization or amplitude of light, either through reflection or transmission. A reflective SLM acts as a pixelated mirror, where every pixel can be individually addressed to modulate the reflected light [72]. A transmission SLM works similarly, but it is implemented like a filter. Applications include optical tweezers [73], and image projection, among many other things [74]. By use of a lens system, the SLM can be placed in the Fourier plane of an imaging system, and can there be used to project images, by using the Fourier transform of said image on the SLM, or to emulate filters. A simple setup using a SLM is shown in Figure 2.9. Note that the laser is focused at the SLM, which causes a very high intensity in a small spot. This can lead to permanent damage on the SLM if intensities exceeding the damage threshold are used [75].

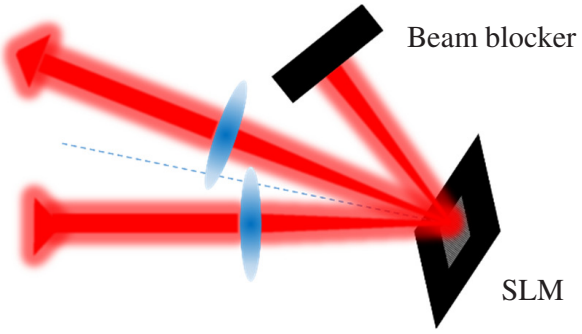

Figure 2.9. A SLM in the Fourier plane of an imaging system, allowing it to be used as a spatial filter. Dashed line is normal to the SLM surface.

2.5 Fluorescence lifetime imaging microscopy

Fluorescence lifetime imaging microscopy (FLIM) is an extension of time-resolved fluorescence spectroscopy and TCSPC, which brings the techniques into the imaging domain through the combination with laser scanning microscopy. By utilizing the fluorescence decay time specific to different fluorescent compounds, further information about the studied specimen can be acquired.

By using fast detectors to measure the time between the pulse and the detected photon for a large number of pulses and photons, a probability distribution can be obtained. The fluorescence lifetimes can now be calculated from these curves by fitting exponential functions to it. The functions have the form

$$I = a_0 e^{-\frac{t}{\tau_0}} + a_1 e^{-\frac{t}{\tau_1}} + \ldots, \tag{7}$$

where I is the intensity at time t, a_n is the intensity just after the pulse and τ_n is the lifetime of the n-th fluorophore. Several decay curves have to be fitted to the distribution, one for each fluorophore that is being detected, and are usually calculated as the slope of $\log(I(t))$ versus t [69, 76]. As illustrated in Figure 2.10, the information about the decay times can be used to color code the intensity image, providing a new dimension of information. Using the acquired information in this way, information about the chemical composition of the sample can be gained, and for example, two fluorophores which overlap spectrally, might be distinguishable.

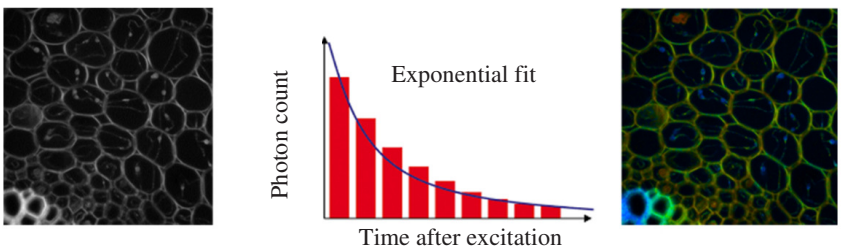

Figure 2.10. As each pixel in the intensity image contains time-resolved data, a new image can be generated from this data, in which the color provides information about the decay time of the corresponding pixel, while the brightness of each pixel still corresponds to the photon intensity.

There are several techniques available to achieve FLIM. In the gated approach, photons from a single laser pulse are only detected after a variable delay, and after several pulses with different delays, the decay time for the region of interest can be determined [77]. In time-correlated single-photon counting (TCSPC), the time between the excitation laser pulse and the detected photons are measured for many pulses [69]. TCSPC allows for collection of photons from several locations in parallel, which is useful for speeding up imaging.

Fluorescence lifetime imaging is a powerful tool, as the lifetimes are insensitive to the actual concentration of the fluorophore but rather dependent on the state and environment of the fluorophore. So far, FLIM of skin has been adopted to assess the metabolic state of biological tissue in response to changes in the microenvironment based on changes in the life-time of tissue autofluorescence [78]. FLIM also allows the detection of changes in pH, ion concentration, and Förster resonance energy transfer (FRET) [79]. FLIM in connection to *in vivo* CLSM has been performed to assess fluorescence lifetime of acriflavine administered to skin [80]. In addition, FLIM has been applied for investigating cellular update of novel photosensitizers [81]. Although the technique is currently restricted to investigative studies, it demonstrates great potential in determining how cellular accumulation of novel photosensitizers takes place.

The experimental system developed has been equipped with data collection hardware capable of performing FLIM. This is achieved by reading the detectors at a high speed (10 MHz) and correlating the time of the detected photon with a sync pulse from a photodiode at the laser cavity. Chapter 5.3 includes FLIM images acquired using the system.

2.6 Gold nanoparticles

Gold nanoparticles (AuNPs) refer to particles of gold with a diameter on a 1-100 nm scale. AuNPs demonstrate potentials for a wide variety of applications[82] due to their special features and the possibilities of tailoring their optical properties. AuNPs were previously introduced as immunolabeling contrast agents for transmission and scanning electron microscopy [83-86]. AuNPs are also an attractive method for drug delivery [33, 87, 88] and are explored for the purpose of photothermal cancer treatment [89-91].

Just like molecules can absorb photons through the excitation of electrons, nanoparticles of noble metals can absorb photons through localized surface plasmon resonance (LSPR), a coherent oscillation of the surface conduction electrons [92]. For a nanoparticle with a diameter of 20 nm, this absorption has a maximum at 525 nm. The characteristics of the absorption is highly dependent on the size and shape of the particles. Bringing two or more particles together will further change the characteristics through “plasmon coupling”, in which the two particle’s electrons can form a larger electron cloud, capable of absorbing new wavelengths [93].

A major difference from molecules is that while molecules have distinct energy levels, the AuNPs have energy bands, much like most metal bulk systems. For bulk gold, these form a quasi-continuous band structure, but as the particle size shrinks, the bands become more and more separated. For AuNPs, there is a band-gap between the outermost conducting band, and the remaining bands, which gives rise to many of the properties which differentiate AuNPs from gold in bulk state [93, 94].

While AuNPs in themselves carry many interesting properties, these can be expanded further by coating the surface of the particle with another substance. By coating the particles with Poly(ethylene glycol) (PEG) [95], or thiol compounds [96], the particles can be made more stable. Functionalization can also be used to prevent or facilitate aggregation. By using secondary anti-bodies in the coating, the AuNPs can be made to aggregate around desired features in the

sample. They can then be used for image contrast in techniques such as SEM [97].

The color of AuNPs in solution depends strongly on the size and configuration of the particles. Aggregation of AuNPs causes a visible shift in the LSPR, in which the peak is red-shifted [98-100], which can be seen in Figure 2.11. This effect can be used as a way to measure particle size [101]. Functionalized AuNPs are used in some home pregnancy tests, among many other things.

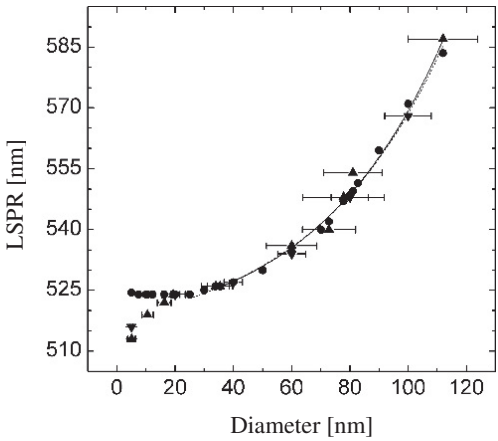

Figure 2.11. The LSPR position as a function of AuNP size. Circles show calculated values and triangles measured. Reprinted with permission from [102]. Copyright 2007 American Chemical Society.

2.7 Multiphoton induced luminescence

When exposed to high photon densities, there exists a probability that metal nanoparticles will absorb multiple photons and exhibit multiphoton induced luminescence (MIL). This effect was first observed when studying second harmonics generation in roughened noble metals [103]. MIL is not detected from bulk metals, due to the continuous distribution of energy levels [104]. However, it is clearly visible in nanoparticles, where the small size forces a gap between the conducting and the valence band. Due to the dynamic nature of the process, no sharp peaks are seen in the emitted spectrum [104, 105]. MIL is thoroughly described in Section 3.2.

The lack of fluorescence when using MPM to image 10 nm AuNPs in solution led to further explorations of the particle system. More specifically, the role of the internal configuration of the particles on the generated MIL signal was investigated using AuNPs deposited in a gradient on a substrate (Paper II). Further studies were made on functionalized AuNPs in solution, with an internal configuration which could be controlled chemically (Paper III).

3 Theory and hypothesis

This chapter is intended as an introduction to concepts used throughout the thesis, and provide a theoretical background and hypothesis to the studies which have been carried out.

3.1 Annular beams

To increase imaging depth, the laser intensity can be increased for a stronger signal. This increases the risk of out-of-focus signal, as discussed in Section 2.3.2.3. If the photons are spread over a larger area, as in an annular beam, the peak intensity outside of the focal volume will decrease, thus decreasing the out-of-focus signal, as illustrated in Figure 3.1. The remaining out-of-focus signal generated should only originate from molecules located away from the optical axis, where the collection efficiency of the objective is lower. When the central part of a laser beam is blocked or diverted to the sides of the beam, a hole is created in the middle, and the beam is referred to as annular. When the blocked portion of the beam becomes large in comparison to the full radius of the beam, annular beams form focal volumes approaching the self-regenerating Bessel beams, and will always show an elongated focal volume compared to a Gaussian beam when focused through a microscope objective [41].

Annular beams have previously been explored for biological applications, and the elongated focal volume is used in MPM with extended field of view [106, 107]. It has also been concluded that annular beams can be used to improve the resolution of laser scanning microscopy [40, 42]. However, this is the first time annular beams are explored for the purpose of reducing the out-of-focus fluorescence.

To understand how the annular beam behaves in a MPM, two sets of computational models were implemented. In the first set, the behavior of the beam as it entered the sample was investigated through a geometric approach; in the second, the shape of the focal volume was computed using the Fresnel-Kirchhoff approximation. In both sets, the inner radius of the annular beam was varied. The variables and

coordinates used to describe the focusing beam can be found in Figure 3.2.

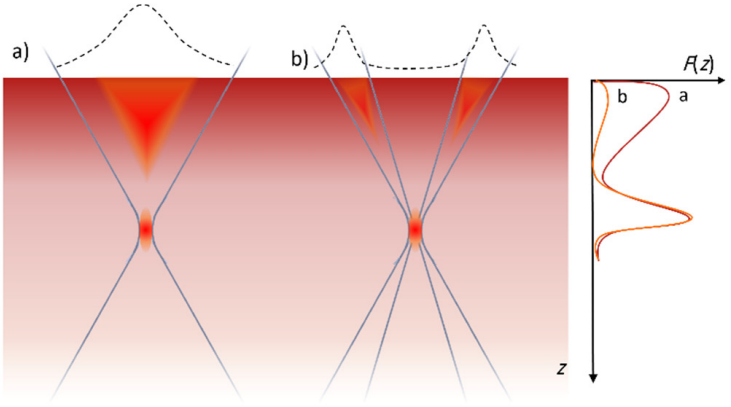

Figure 3.1. A comparison between the profiles, taken along the optical axis, of a) a Gaussian and b) an annular beam. *F(z)* show a hypothetical distribution of out-of-focus fluorescence. Image not to scale.

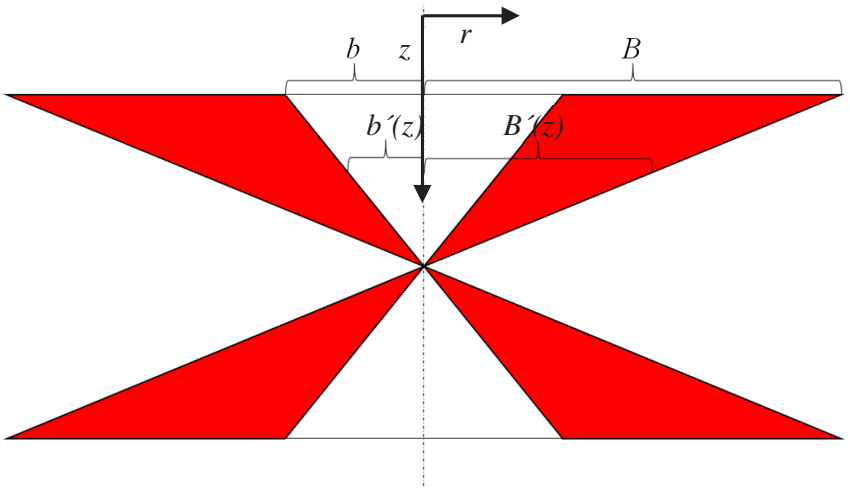

Figure 3.2. A reference for the variables and coordinates used to describe the beam radius as the beam focuses.

3.1.1 The geometrical approach

The radial Gaussian beam intensity profile is described, using coordinates from Figure 3.2, by

$$\Psi'(z) = \frac{P_0}{\pi B'^2} e^{-2\left(\frac{r'}{B'}\right)^2}, \tag{8}$$

where P_0 is the peak power, r' is the radial coordinate and B' is the beam width, which decreases as a function of the depth z through the relation

$$B'(z) = B\left(1 - \frac{z \tan \alpha}{a_0}\right). \tag{9}$$

Here, B is the beam width at the aperture exit, a_0 is the aperture radius and α is calculated from the NA (cf. eq. 3, p.12)

The radial annular beam intensity profile at depth z is described by

$$\Psi'(z) = \frac{P_0}{\pi B'^2}\left(1 - \frac{b'}{r'}\right) e^{-2\left(\frac{r'-b'}{B'}\right)^2}, \tag{10}$$

with the addition of b', a parameter describing the inner radius of the annular beam. In this simulation, the variable b' depends directly on z in the same way as B' and is defined as

$$b'(z) = b\left(1 - \frac{z \tan \alpha}{a_0}\right), \tag{11}$$

where b is the radius of the missing disk of laser light in the center of the beam at the aperture. The relation b/B, i.e. the relation between the inner radius and the full radius of the beam at the lens is used to characterize an annular beam throughout the thesis.

3.1.2 The Fresnel-Kirchhoff integral

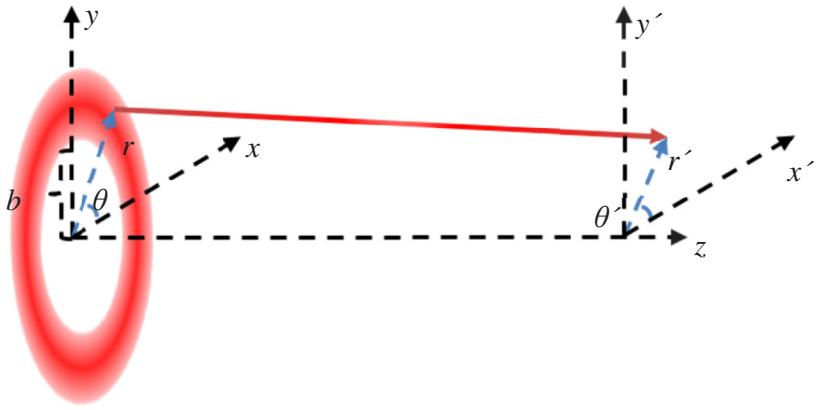

Figure 3.3. The coordinates used in the Fresnel-Kirchhoff integral. For every point ($r´$, $\theta´$, z) located at a distance from the lens, the contribution from each area element (r, θ) on the lens is added. The area on the lens is limited by the full beam radius and the inner diameter of the beam (b).

The Fresnel Kirchhoff integral [43] can be used to calculate the contribution of a light source to a single point, by modelling the source as a collection of point sources and summing the contribution from each of these point sources, as illustrated in Figure 3.3. The form used in this thesis is adapted from work by Liu *et al.* [108]. The integral is given by

$$\Psi'_{fk}(r',\theta',z) = \frac{2\pi}{z\lambda}\int \Psi'(r,\theta,0)e^{\left(\frac{-2\pi iR}{\lambda}\right)}\Phi_l dS, \qquad (12)$$

where λ is the wavelength of the laser, $\Psi´$ is the field amplitude at a point on the lens, modelled as in eq. 10. Φ_l is the phase retardation of the lens calculated as

$$\Phi_l = e^{\frac{i\pi r^2}{\lambda f}}, \tag{13}$$

where r is the radius coordinate on the lens, and f is the focal length of the lens. Figure 3.3 provides a visual guide to the variables used.

R is the distance between the point in space (r', θ', z) and the area element (r, θ) on the lens surface.

$$R \approx z + \frac{r^2 + r'^2 - 2rr'\cos(\theta - \theta')}{2z} \tag{14}$$

In the case of annular beams, all of these equations are combined to obtain the following equation:

$$\Psi'_{fk}(r', \theta', z) = E_0 \frac{2\pi}{\lambda z} \int_b^B \left(1 - \frac{b}{r}\right)^{1/2} e^{-\frac{1}{2}\left(\frac{r-b}{B}\right)} e^{\left[ik\left(\frac{r'^2}{2f} - z - \frac{r'^2 + r^2}{2z}\right)\right]} J_0\left(\frac{2\pi r' r}{\lambda z}\right) r dr \tag{15}$$

E_0 is a constant. $J_0(x) = \frac{1}{2\pi}\int_0^{2\pi} e^{ix\cos(\theta - \theta')}\, d\theta$ is a zeroth order Bessel function of the first kind.

In Paper I, simulations were made to evaluate the effect of annular beams on the focal volume and out-of-focus fluorescence in MPM. In Paper IV, annular beams were implemented in an experimental MPM setup to evaluate the method experimentally on phantoms and excised biological specimens.

3.2 Theory of MIL

MIL differs from multiphoton absorption in fluorophores in that it is not a simultaneous absorption of the photons, but rather a sequential absorption of multiple photons. The absorption is followed by photoluminescence caused by recombination of conduction band electrons with holes in the *d*-band [105, 109, 110]. This is illustrated in Figure 3.4. During the absorption of the first photon, one electron from the partially filled *sp*-band is excited above the Fermi-level, leaving an electron hole. This intra-band transition is interpreted to be related to the excitations of the plasmon (as will be further discussed below). The hole in the *sp*-band is subsequently filled by an electron that is excited from the *d*-band by the sequential absorption of a second photon and can be considered a single particle excitation. The sequential process creates an excited system, with energy greater than the incoming photon-energy. In competition with other thermalization processes, the excited *d*-hole can decay radiatively giving rise to luminescence [110, 111]. When the hole in the *d*-band is recombined with the excited electron in the *sp*-band, a photon with greater energy than that of the single exciting photons is emitted. The sequential two-photon induced luminescence can be described by [110]

$$\frac{dN_{sp}}{dt} = \sigma_{sp\rightarrow sp} N F(t) - \frac{N_{sp}}{\tau_{sp}} - \sigma_{d\rightarrow sp} N_{sp} F(t) \tag{16}$$

and

$$\frac{dN_d}{dt} = \sigma_{d\rightarrow sp} N_{sp} F(t) - \frac{N_d}{\tau_d}. \tag{17}$$

N is the electron density in the *sp*-band, N_{sp} and N_d are the densities of holes created below the Fermi-level in the *sp* and *d*-bands respectively. τ_{sp} and τ_d are the relaxation times of the *sp* and *d*-holes. $F(t)$ is the photon flux and $\sigma_{sp->sp}$ and $\sigma_{d->sp}$ represent the cross sections of first and second absorption event. The third term in (17) can be neglected as $N_{sp} << N$. By changing the pulse length of the

exciting photons, the sequential process can be tuned between two-, three-, and four-photon processes [93, 110, 112, 113]

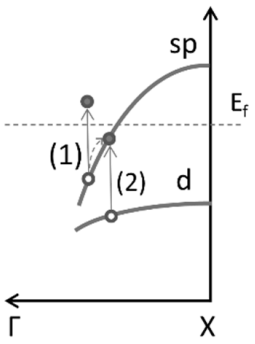

Figure 3.4 Schematic diagram of the band structure near the X symmetry point of Au illustrating the sequential absorption of two-photons as introduced by Imura *et al.*(24) The first photon excites an electron from the conducting *sp*-band (1), leaving behind a hole which is filled via the excitation of an electron from the *d*-band (2). The dashed line indicates the Fermi surface.

Unexpected results acquired during separate experiments performed by the Ericson group indicated that spherical AuNPs in solution do not exhibit MIL, while a MIL signal was present after the particles had been deposited on a substrate. It has been shown that there exists a connection between the plasmon resonances and the shape of the AuNP [98-100, 104, 114, 115]. This led to the hypothesis that the electron clouds surrounding the AuNPs can couple when in close proximity, allowing the particles to act together with the absorption properties of a larger particle. This is in line with earlier observations [109, 116] demonstrating that the plasmon along the long axis of gold nanorods is resonantly coupled to the photoinduced luminescence. It was hypothesized that the MIL signal from spherical AuNPs could be controlled by controlling the inter-particle configuration, which was explored in Paper II and III.

4 Methods

The aim of this chapter is to provide an overview of the methods used for the studies. A more thoroughly description can be found in the papers supplemented at the end of the thesis.

4.1 Mathematical modelling of annular beams

To ensure the performance of the annular beams in a MPM setup, simulations were performed. In the first set, the generated background was computed through a rough, geometric approach, and in the second a high-resolution image of the focal volume was calculated, as described in Section 3.1. Both models were evaluated using a range of different annular beam parameters. It is important to know how the focal volume changes with the shape of the beam, as this shape directly determines the resolution of the system.

4.1.1 The geometric approach

In the geometric approach, the beams were modeled as they entered the sample, before the focal plane, to determine the generated out-of-focus fluorescence. The two different sets of beams were described by equations of their respective radial profile, as described earlier in Section 3.1. No angular dependency was introduced in either beam. Examples of the beams can be found in Figure 4.1.

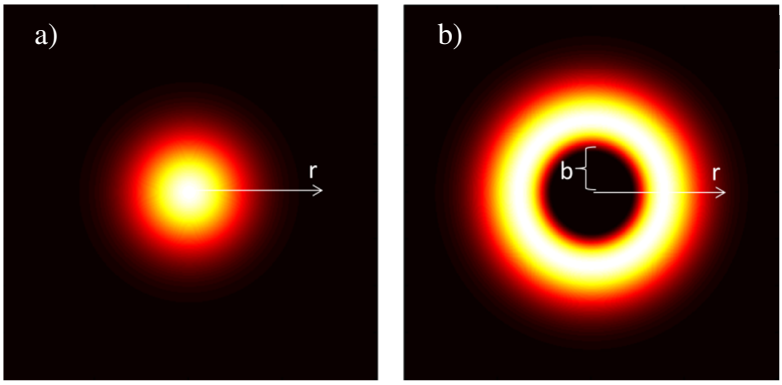

Figure 4.1. Examples of a mathematical representation of a) a Gaussian beam, and b) an annular beam. The variable *b* represents the size of the blocked part of the beam. Intensities are normalized to the peak values of each image for clarity.

A series of simulations were performed for different values of *b* by letting *z* vary from 0 (the objective aperture, exit diameter: 2 mm) to a value very close (93%) to the focal distance (2.7 mm, NA=0.8) of the objective. In this model, a homogenous media is introduced between the objective and the sample volume, and corrections are made for light attenuation by exponential factors which depended on *z*. The values for these attenuation functions (150 cm^{-1}) were based on work performed by Meglinski *et al.* [117]. It has been shown that scattered light does not contribute to the multiphoton processes and scattered light is therefore not taken into account. Instead, only ballistic photons are considered [118].

4.1.2 Mathematical modelling of the focal volume

To calculate the shape of the focal volume, a second set of simulations were performed using the mathematical model described in 3.1.1 and the integral described in 3.1.2. The coordinates used in the model are shown in Figure 3.3.

The Fresnel-Kirchhoff integral was calculated on a grid (6 x 6 um, 2001 x 2001 points) around the focus of the laser. In short, the contribution from each part of the annular beam as it passed through the objective lens was added in each pixel around the focal volume,

with phase taken into account. Since the result is rotationally symmetrical, only r and z were varied during every run. The inner diameter b and the NA of the objective were varied over several runs from 0 to 1 with 0.01 increments. Values for the variables were taken from the MPM set-up (exit aperture: 2 mm, NA = 0.8, n=1.33, λ = 800 nm). The model assumes linearly polarized light, which is also used in the experimental set-up, but does not take attenuation into account due to the short z-interval considered.

The Bessel function identity was used to reduce computation time by allowing MATLAB's built-in function for Bessel functions. The calculations were carried out using MATLAB R2010b (Mathworks, Natick, MA). The code used is appended as Appendix A. The models described are evaluated in Paper I and form the basis of the experiments described in Paper IV.

4.1.3 Data analysis (simulations)

Data was collected as intensity matrixes in MATLAB, and analyzed using the same software. Out-of-focus fluorescence was calculated by squaring the pixel intensities at each z-level account for the non-linear dependency of the fluorescence on the excitation light. The signal contribution from each z-level was then summed. The size of the focal volume was determined by finding the full-width-half-maximum of the volume along the z and r-axis.

4.2 Imaging gold nanoparticles

To be able to investigate how the MIL signal depends on aggregation, and explore the feasibility of an AuNP-based, chemically switchable, contrast media, two different systems were studied; Plates with AuNPs deposited in a gradient (Paper II), and functionalized AuNPs in a solution (Paper III).

4.2.1 AuNP gradient plates

AuNP gradient plates used in Paper II were acquired from Cline Scientific [119, 120] to be used in MIL experiments. The plates, initially designed to be used for cell culture experiments, were covered with 10 nm AuNPs, chemically disposed in a concentration gradient across the plate [119, 120]. The gradient plate production process is illustrated in Figure 4.2. In reality, the gradient plates are square.

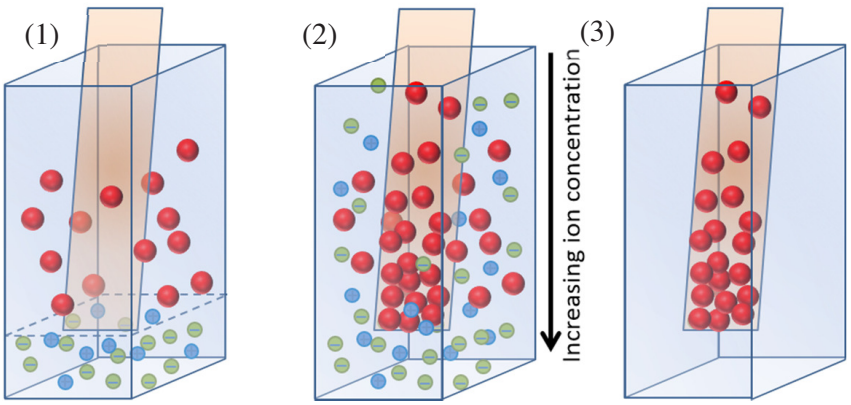

Figure 4.2. Gradient plates were produced by placing a gold substrate modified with dithiols is vertically in a cuvette filled with a AuNP solution having low ionic strength (red spheres in the image) [119, 121]. A buffer with high ionic strength (green and blue spheres) is then layered below the particle solution below the edge of the substrate (1), whereupon the ions diffused (2) upwards triggering a backfill of particles on the surface (3). Reprinted with permission from Paper II, supplementary materials.

The controlled distribution of particles in a gradient on the plates made them suitable for investigations on how MIL depends on particle

concentration and inter-particle distance. Through scanning electron microscopy (SEM) images of reference plates it could be concluded that the particles were clustered in the regions with high particle concentration. Clustering was also seen in the region with the lowest concentration, where a uniform and low concentration was expected. Figure 4.3 shows SEM-images of the plates at three different locations and particle coverage.

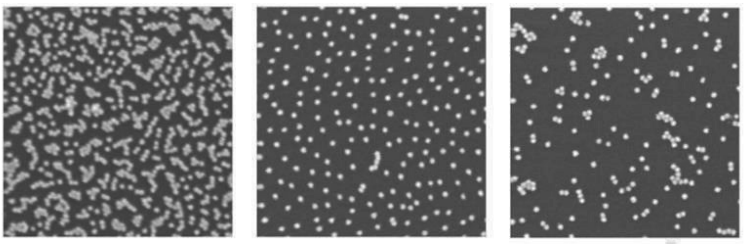

Figure 4.3. SEM images showing the nanoparticle distribution at three different sites. Note that clustering is present at high concentrations, as well as low concentrations, while the intermediate concentration exhibits little clustering. Field of view for each image: 525 x 525 nm.

The gradient plates were imaged using a commercially available MPM (LSM 710 NLO microscope system, Carl Zeiss MicroImaging GmbH, Germany), together with a Mai Tai DeepSee tunable NIR Ti:Sapphire fs-laser (Spectra-Physics, Newport Corporation, USA). Two Plan-Apochromat 20x/1.0 water immersion objective lenses were used in the experiments, one lens corrected for a 0.17 mm cover glass, and in later experiments, one water immersion lens without cover glass correction. Measurements were performed either by mounting the gradient plates between an objective glass and a cover glass using a custom-made imaging chamber, or directly using the water immersion lens.

The substrates were placed in the microscope and systematically investigated by starting in the area with the highest particle coverage and moving towards areas with lower coverage. The laser powers used ranged from 7.5 mW to 13.5 mW measured at the back aperture of the objective lens, depending on experiment and position along the substrate. The field of view was 386 x 386 µm. Tiling was performed to achieve an assembled image across the whole gradient plate.

The signal, and the originating process, was characterized by looking at to which power the signal depend on the excitation energy. The characterization experiments were performed by imaging the samples using varying levels of intensity and recording the signal level. A logarithm taken of both sides then reveals the power dependency of the signal on the excitation energy. A value above 1 indicate a non-linear process. This is expressed as

$$F_{MIL} = aI^x \quad (18)$$

$$\log F_{MIL} = \log a + x\log I, \quad (19)$$

where F_{MIL} is the measured signal, a is a constant, I is the laser intensity and x is the power dependency to be determined. When the logarithms are plotted against each other, the power dependency x can be read as the slope of the plot.

The dependency of the MIL signal on the clustering was evaluated by comparing the power dependency of the signal on the incoming laser light at different locations along the gradient. The degree of clustering and particle density as a function of gradient coordinate was calculated from SEM images provided, using MATLAB. AFM (Dimension 3100, Veeco Digital Instruments/Bruker) measurements were performed to confirm the particle distributions read from the SEM images supplied by the manufacturers of the plates.

4.2.2 Functionalized AuNPs

AuNPs functionalized using *de novo* peptides (JR2EC) [2] suspended in a Bis-Tris buffer were used to further explore how the effect of clustering on signal could be utilized. The particles cluster in the presence of Zinc ions (Zn^{2+}) or when the pH deviates from 7. Several other di- and tri-valent metal ions induces folding. However, Zn^{2+} has been found to give the strongest effect [122]. Subsequent addition of EDTA to the solution containing Zn^{2+} shields the Zn^{2+} from the

[2] Originally developed by Johan Rydberg and Sarojini Viyayalekshmi, and further refined by Karin Enander and Daniel Aili at Linköping University.

peptide and reverses the aggregation [122, 123]. The particles have already been explored for the purpose zinc sensing [124] and phosphatase activity detection [125]. Three experiments were prepared, using different configurations of chemicals and AuNPs.

Table 1. The experiments prepared to test the dependency of MIL on AuNP aggregation.

Expected configuration	**Contents**
Dispersed particles	AuNPs, Bis-Tris buffer solution
Aggregated particles	AuNPs, Zn^{2+}, Bis-Tris buffer solution
Particles with reversed aggregation	AuNPs, Zn^{2+}, EDTA, Bis-Tris buffer solution

By forcing the particles to cluster, as illustrated in Figure 4.4, the particles could be made to absorb the excitation light and exhibit MIL. This allowed for a greater control over image contrast.

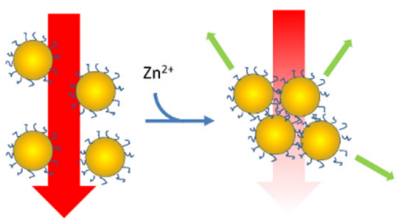

Figure 4.4. The AuNPs aggregate in the presence of Zn^{2+}, allowing the electron clouds to couple and support new plasmon resonance modes, which in turn allows the particles to absorb the incoming laser radiation and generate multiphoton induced luminescence.

The particles were imaged using a commercial MPM (Section 4.2.1), in a custom-made imaging chamber. Additional measurements were performed using the experimental microscopy setup, which will be described in 4.3. Since this setup is inverted, it provided easier access to the sample. The laser power used remained the same as in the previous chapter (7.5 mW to 13.5 mW measured at the back aperture)

and a wavelength of 800 nm was used to acquire several 3D-stacks of images from each sample. UV-Vis spectra were acquired from all samples to monitor the plasmon peak shift associated with clustering of AuNPs [98-100], using a Cary 50 Bio (Varian).

It was noted that the signal level increased from particles which were repeatedly exposed to the focused laser beam, suggesting a structure change. This was confirmed using TEM instruments on particle clusters which were allowed to sediment on to TEM-grids and then repeatedly imaged.

4.2.3 Data analysis (AuNPs)

Data from the imaging of AuNPs was collected as .lsm-files (Carl Zeiss MicroImaging GmbH, Germany) for the commercial MPM used in Paper II and III. Data was exported using Zen 2011 (Carl Zeiss MicroImaging GmbH, Germany) as greyscale images and analyzed using imageJ (NIH) and MATLAB to determine average intensity and slope values (see 4.2.1). Data from the inverted setup used in Paper III was collected as .sdt-files using SPCM (Becker&Hickl, Germany). This file format is capable of storing the full FLIM-information of the image. As only the intensity was of interest, the images were exported as intensity matrixes using SPCImage (Becker&Hickl, Germany) for further analysis in imageJ.

4.3 Experimental MPM

An experimental multiphoton setup was designed and constructed primarily with the aim of implementing annular beam and evaluating the mathematical models discussed in 4.1, in a series of experiments. The system allows for a multitude of different techniques, such as FLIM and FCS. A schematic image and a photo of the system are shown in Figure 4.5 and Figure 4.6, respectively. The system parts are listed in Table 2.

Table 2. Microscope components, in the order they appear in the signal path.

Component	Model, Manufacturer	Specification
Pulsed laser	Tsunami, Spectra physics	80 Hz, 700-1050 nm
Photodiode	APS-100-01, Becker&Hickl	
Pockels cell	350-80LA, ConOptics	
Beam expander	BE05M-B, Thorlabs	5x magnification
Half-wave plate	WPH10E-808, Thorlabs	808 nm
Spatial light modulator	X10468-02 Lcos-SLM	800 ± 50 nm
Galvo mirror system	GVS002, Thorlabs	5 mm diameter
Microscope objective	C "Achroplan" NIR, Carl Zeiss Olympus UPlanFLN	40x/0,8W D=0,17 10x/0.30
Filters	Semrock, Brightline	447/60 nm 525/50 nm 580/150 nm
Photo-multiplier tubes	2x H7422P-40 MOD, Hamamatsu	300 - 720 nm
Data collection cards	SPC-150, Becker&Hickl	10 MHz
Software	SPCM, Becker&Hickl	V.9.67

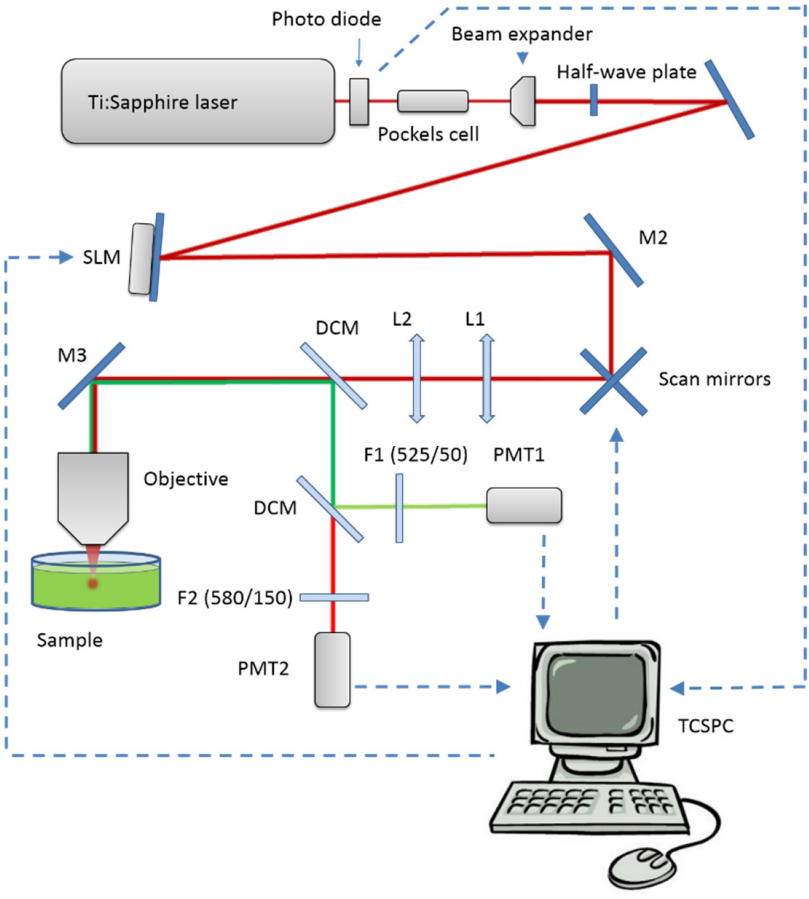

Figure 4.5. Schematic of the experimental MPM setup. It compromised of a pulsed laser, a Pockels cell for intensity modulation, a beam expander and scan mirrors to scan the beam across the sample. The laser is focused with an objective, which also leads the signal back to the detectors (PMTs). The setup include mirrors (M1-2), lenses (L1-2), dichroic mirrors (DCM) and filters (F1-2). A Pockels cell provides a way to modulate the intensity of the laser through a voltage applied over a crystal.

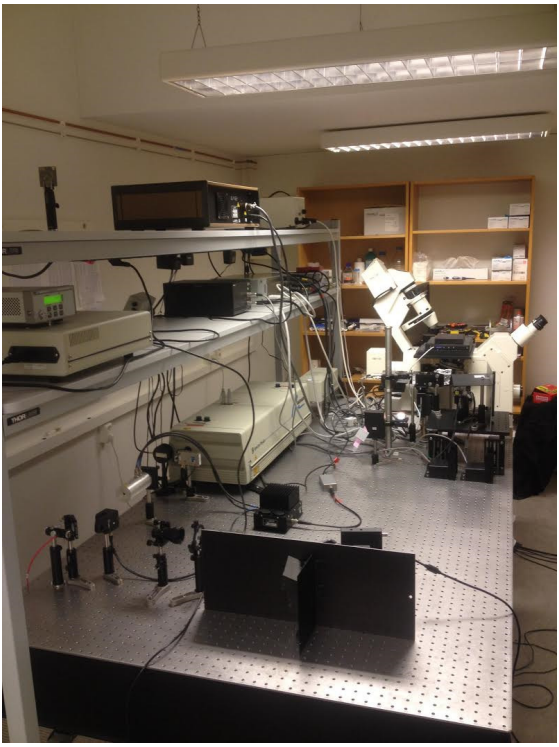

Figure 4.6. The experimental MPM setup, with the laser coming towards the camera in the left of the picture before being reflected to the right through the beam expander and back towards the scanning mirrors and the microscope body.

4.3.1 Implementation of annular beams

Initially, a beam-blocker was used to create an annular beam (Paper I). A microscope slide with a small dot of black paint was used to physically block the center of the beam. While this caused the beam to become annular, it also introduced diffraction problems, and while cheap, was difficult to control. A set of experiments were performed using the beam-blocker.

For the following studies (Paper IV), a phase-only SLM, introduced in Section 2.4, was used to modulate the incoming light into an annular beam. Several works already details the creation of annular beams using SLMs, for the purpose of i.e. laser drilling[126], and for STED

microscopy [3, 127]. However, both of these application use beams less suitable as an excitation source, as they are either non-collimated or does not focus to a point. Instead, in this study, a collimated beam was created by deflecting the beam in the areas where no intensity was desired. The pattern used is shown in Figure 4.7. The triangular-wave-like areas causes a gradient shift in the phase of the reflected light, which changes the direction of the wave-front through interference. The undesired part of the beam is directed towards a beam-blocker. Approximately 25% of the laser power is deflected in this process. Increasing the initial laser power can compensate for this.

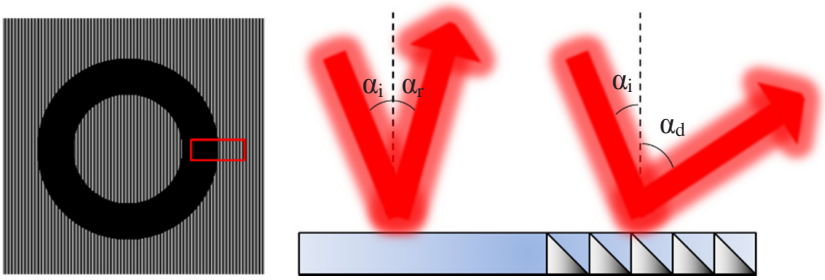

Figure 4.7. A phase-pattern used on the SLM to deflect unwanted intensity to the side. The light hitting the black areas in unaltered and reflected further into the microscope. $\alpha_i = \alpha_r \neq \alpha_d$.

Several approaches for creating an annular beam using a SLM were evaluated. While using a Fourier transform of a ring as a pattern successfully created a ring-shaped beam, the beam was focused and diverged beyond the focusing plane, rendering this approach sub-optimal.

By using a more direct approach, in which a ring was created by reflecting the desired parts of the beam while intentionally scrambling the other parts, a more collimated annular beam could be created. The shape of the beam was evaluated using a beam profiler placed at the back aperture.

4.3.1.1 Power matching

When the central part of the laser beam is blocked or diverted, intensity is naturally lost. To compensate for this, the initial intensity was increased by lowering the voltage over the Pockels cell. Calibration curves were created by measuring the intensity at the back aperture for annular and Gaussian beams respectively. One such curve, made for an annular beam with *b/B*=0.4, is shown in Figure 4.8. As can be seen, the intensity loss at the back aperture can easily be compensated for by adjusting the Pockels cell, and thereby changing the intensity before the SLM.

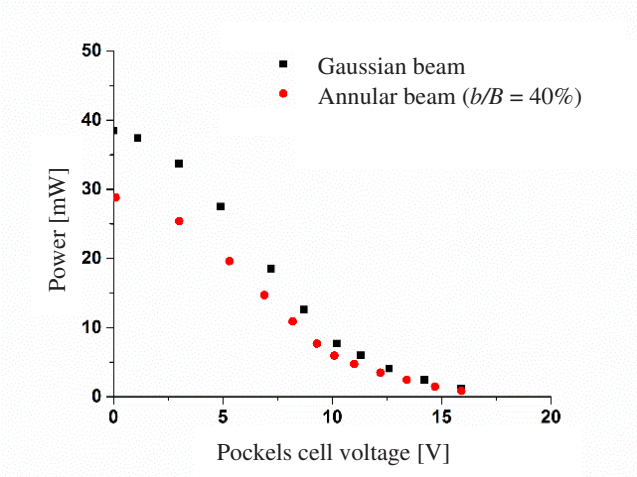

Figure 4.8. A calibration curve showing the intensity at the back aperture when using a set voltage at the Pockels cell and an annular beam (*b/B*=0.4) and a Gaussian beam respectively.

4.3.2 Custom data collection and software

During the development of the experimental system, custom-made detector read-out and data collection software was implemented using a FPGA. The detectors were connected to a pre-amplifier, which in turn was read using a modular system based around a field-programmable gate array (FPGA) module (NI cRIO-9075, National Instruments). An input module (NI cRIO-9205) was connected and

controlled by the FPGA, which reads the pre-amplifier and transmits the data to the software.

Custom software was designed using LabVIEW to allow the user to control settings for the image and save the collected data. The interface is shown in Figure 4.9. While simple, it provides functionality, such as physical zoom and live histogram manipulation.

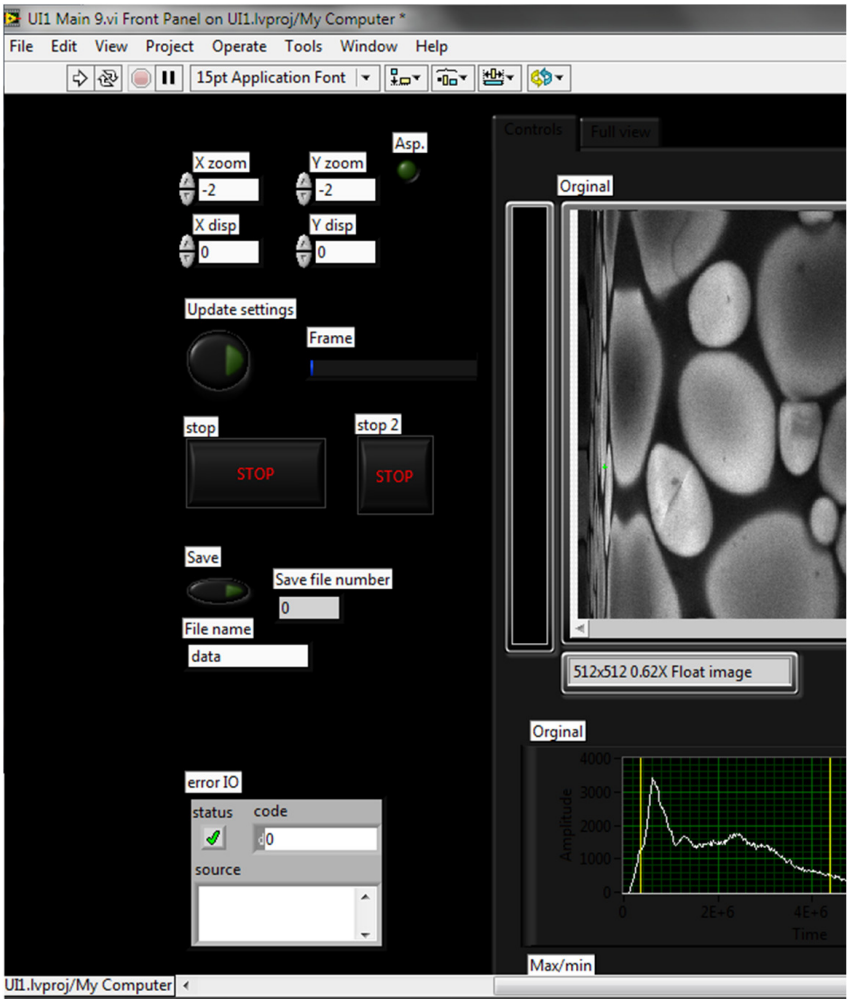

Figure 4.9. The custom interface designed in LabVIEW. It features controls for zoom and displacement of the beam as well as histogram modifications and file saving. The distortion in the right side of the collected images is from data collected during mirror fly-back. Image shows starch grains stained with rhodamine B.

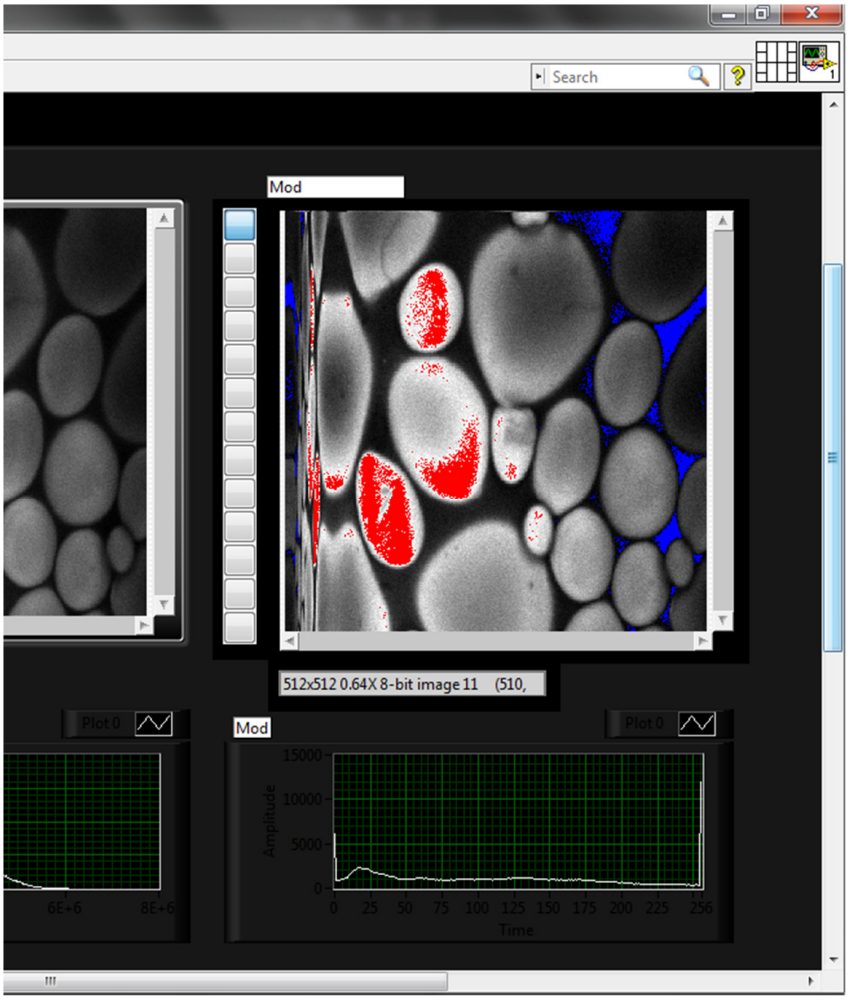

While the custom software has been replaced with commercial software capable of TCSPC and FLIM, its design and implementation has provided valuable knowledge in LabVIEW software design, as well as the basic functionalities of a MPM system. This knowledge has proven especially useful for understanding the results from the FLIM system.

4.3.3 Implementation of commercial software

The detectors used in the experimental setup are capable of TCSPC, allowing the acquisition of FLIM images using the technique detailed in Chapter 2.5. The acquisition of FLIM images requires high-speed data collection hardware and software. Two data collection cards (SPC-150) were bought from Becker&Hickl. In addition, hardware to control the scan mirrors (GVD – 120), and software (SPCM) for data collection and analysis were acquired. A photo-diode was used to synchronize the software with the laser. The signal was routed through a cable of a length which corresponds to the desired lag to compensate for the time-lag of the synchronization signal. The hardware and software is described in great detail in the hand book available from Becker&Hickl [128], and will not be detailed here.

The new hardware and software have allowed not only the acquisition of FLIM images, but also greater control over how non-FLIM images are collected.

4.3.4 Stage control for image acquisition

The microscope stage (Microstage and nano-ZL500, MadCityLabs) is controllable through LabVIEW software. This allowed for advanced sample control beyond simply finding a new region of interest (ROI). Using software developed within the group, the sample could be moved in set patterns to achieve larger ROIs, using tile scanning, and *z*-stacks. The software facilitates the use of the system for photo-activation samples in controlled and repeatable patterns, and can be used for automating imaging of 96-well plates.

4.3.5 Phantom preparation

To allow for easier access to samples, and to evaluate the effect of different parameters, artificial samples, phantoms, were prepared with properties mimicking those of skin. The phantoms were used to characterize the system.

4.3.5.1 Non-scattering phantoms

Phantoms were prepared by adding agar powder to a solution of fluorescein (1 µM, Sigma-Aldrich) and sub-resolution fluorescent micro-spheres (FluoSpheres® carboxylate- modified microspheres, 0.17 µm, deep red fluorescent (633/660)) in water at 90°C, which forms a gel when cooled. A schematic overview is shown in Figure 4.10. These samples were used to test the parameters of the microscope setup as detailed in Paper I. The purpose of the micro-spheres was to provide a strong fluorescence signal which could be detected in the red channel of the microscope, while the fluorescein simulated the auto-fluorescence from the tissue. When scanning a micro-bead, a portion of the incoming laser light would excite the fluorescein before reaching the focal volume, which generated a detectable green fluorescence, thus mimicking the out-of-focus background fluorescence in skin. These phantoms were simple, and lacked a scattering component.

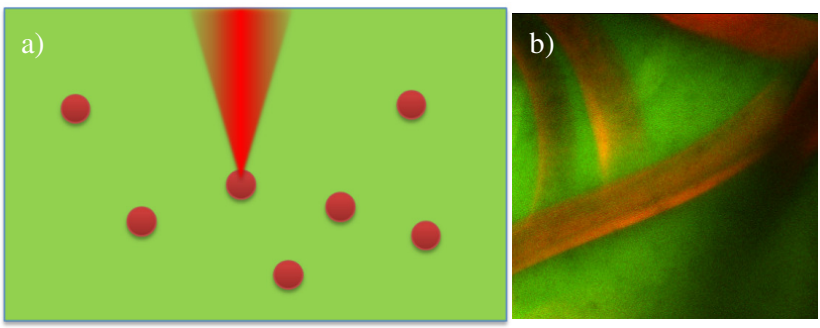

Figure 4.10. a) A schematic figure showing the excitation of a red bead embedded in green gel and b) a MPM image of a scattering phantom. Due to the filters chosen, the green gel's fluorescence signal shows mainly in the green channel, while the red bead's fluorescence shows up mainly in the red channel.

4.3.5.2 Scattering phantoms

To better mimic tissue scattering properties, a similar custom fluorescent scattering phantom was prepared by dissolving 1% weight fraction of agar in 1x PBS. Fluorescein and TiO_2 were added into the

agar solution to yield a 0.1 mM Fluorescein and 10 mg/mL TiO_2 in the phantom. The addition of TiO_2 serves as the scattering component. Through transmission experiments, it could be concluded that this amount corresponds to a scattering of ~40cm^{-1}, approximately 3 times less than a normal epidermal layer of skin [117, 129, 130]). A piece of medical gauze was stained for 5 minutes in a 1 mM RhodamineB-ITC solution at room temperature. The excess staining solution was removed through rising with 1x PBS. The stained gauze was embedded in the agar gel solution, and the solution was allowed to solidify, yielding the final phantom specimen.

4.3.5.3 Skin sample preparation

To evaluate the system's performance when imaging biological tissue, excised normal human skin, acquired from breast reduction surgeries at the Sahlgrenska University hospital, was used in the proof-of-principle experiments. Skin samples were imaged under different conditions including: 1) unstained freshly excised specimen, 2) unstained frozen excised specimen, and 3) RhodamineB-ITC solution stained frozen excised specimen.

For unstained freshly excised specimens, the auto-fluorescence in the epidermis and the dermis were both intact, and visible in the green channel. For unstained frozen excised specimens, the epidermis autofluorescence is lost, but autofluorescence from the collagen fibers in the dermis can be clearly visualized in the green channel. No signal can be seen in the red channel.

In RhodamineB-ITC stained frozen excised specimens, the epidermis is stained and therefore visible in the red channel. Due to the limited penetration of the exogenous fluorescence compound, the dermal layer is not stained by RhodamineB-ITC and does not contribute fluorescence signal to the red channel. The autofluorescence from the collagen fibers in the dermis can be visualized in the green channel. The freshly excised specimens were stored at 4ºC, protected from light. The frozen specimens were stored at -20ºC. Upon completion of the characterization experiments, the skin specimens were discarded according to regulations for biohazardous material defined by the University of Gothenburg.

4.3.6 Data analysis (Annular beams)

Data was collected as .sdt-files using SPCM (Becker&Hickl, Germany) and exported as intensity matrixes using SPCImage (Becker&Hickl, Germany) for further analysis in imageJ and MATLAB. The signal in the red channel originates from a combination of signal from the stained features and cross-talk from the fluorescein background. Similarly, the green channel contain a combination of fluorescein signal and cross-talk. For the purposes of the study, the cross-talk is assumed to be negligible, and a signal-to-background ratio is defined as a ratio between the intensity of the two channels, and used to evaluate the performance of the system.

5 Results

The following chapter contains a summary of the results presented in Paper I-IV, in addition to current work in progress. A more thorough presentation is available in the appended papers.

5.1 Exploring annular beams (Paper I and IV)

The annular beams described in Section 3.1 were implemented on the experimental system described in Section 4.3. Initially, a beam blocker was used to create the annular beams, and the technique was evaluated on non-scattering tissue phantoms (Paper I). The setup was improved upon by exchanging the beam blocker for a SLM, and adding a scattering component to the phantoms (Paper IV). Simulations were made and presented in Paper I, and later improved upon, as presented in Paper IV.

5.1.1 Simulations of the focal volume

Calculations using the geometric approach has shown how the out-of-focus intensity is expected to be distributed in a scattering media after corrections have been made for scattering, absorption, and the signals quadratic dependency on the incoming laser intensity. According to these calculations, the annular approach provides a theoretical reduction of out-of-focus intensity over a Gaussian beam. This effect is a function of the inner diameter, and results are presented in Figure 5.1. It can be seen that the generated out-of-focus fluorescence is less for annular beams with a b/B ratio of around 40%. However, it should be noted that annular beams also changes the focal volume, which is considered in the following simulations.

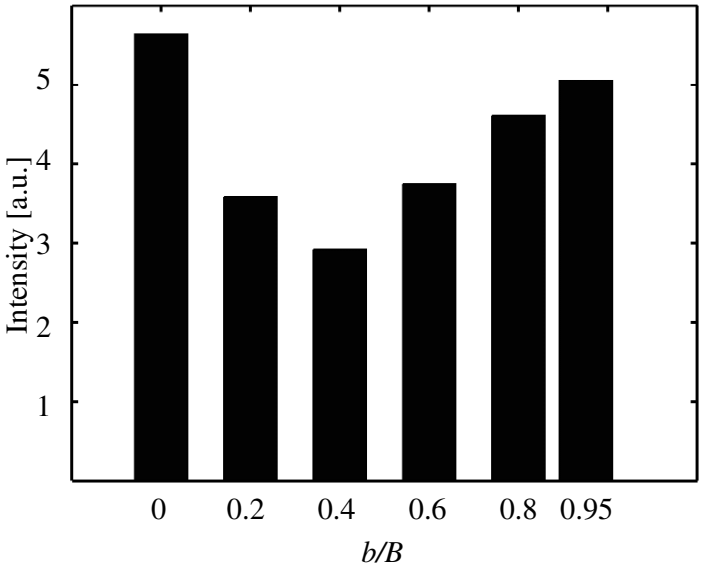

Figure 5.1. The out-of-focus fluorescence generated when focusing a beam of equal intensity, as a function of the *b/B* ratio.

Further calculations were made to ensure that annular beams can produce focal volumes comparable to that of the more commonly used Gaussian beam. The Fresnel-Kirchhoff integral (eq. 12, sec. 4.1.2) was calculated using MATLAB, and some of the result can be seen in Figure 5.2. A series of models were run, and the parameter determining the inner radius of the beam was varied. The axial beam profiles were then compared for the different values and are shown in Figure 5.3. When about 40% of the inner radius was blocked, the beam still produces a focal volume of comparable size to that of a Gaussian beam, while larger values give a significant axial elongation.

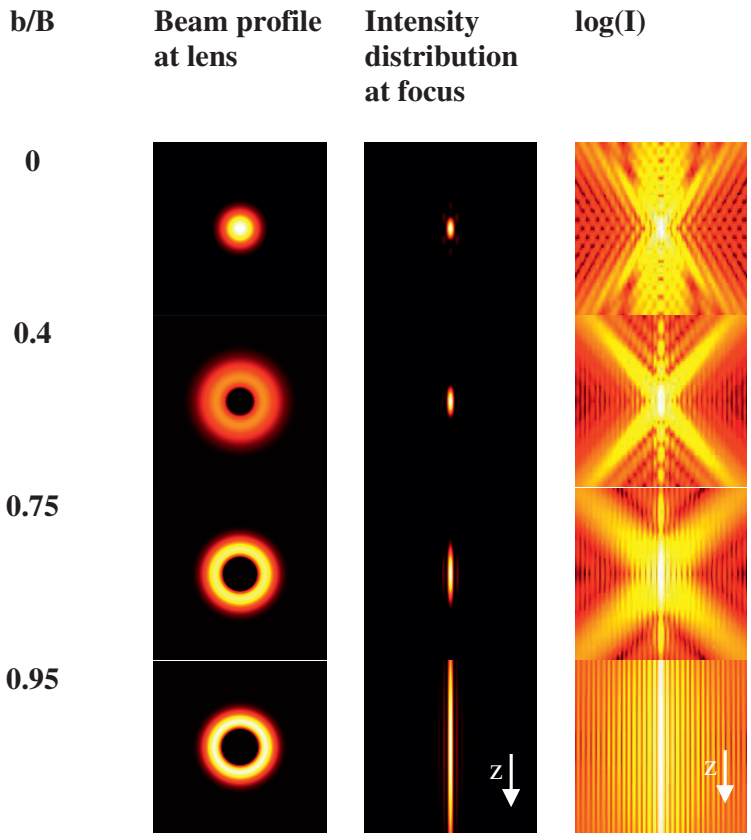

Figure 5.2. The intensity distribution (I) in and around the focal volume for a theoretical simulation of an annular beam where a varied portion of the beam is blocked, as modeled by the Fresnel-Kirchhoff integral.

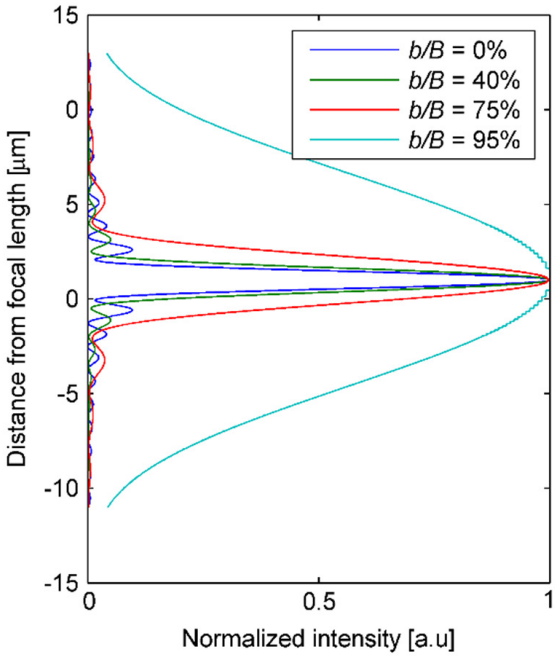

Figure 5.3. The theoretical intensity distribution in and around the focal volume along the optical axis. *b/B* refers to the fraction of the full radius which has been blocked. When the shapes of the profiles are compared, it is clear that a ratio of 40% only marginally affects the beam profile.

5.1.2 Implementation of annular beams

The annular beam setup (described in Chapter 4.3) has been implemented to evaluate the imaging performance in phantoms and excised skin specimens.

5.1.2.1 Beam blocker & non-scattering phantoms (Paper I)

Experiments using the non-scattering phantoms described in Chapter 4.3.5, in combination with a beam blocker, showed a decrease in the background fluorescence when using an annular beam instead of a Gaussian, at the cost of lower peak intensity in the focal volume. These results are shown in Figure 5.4. In this figure, the red channel shows the signal from the beads in the focal plane, which represent the

desired signal. The green channel contains the fluorescence generated from the gel. When the beam scans through a bead, all of the green signal originates from out-of-focus fluorescence. The results show that this undesired signal drops more than the desired signal when using annular beams.

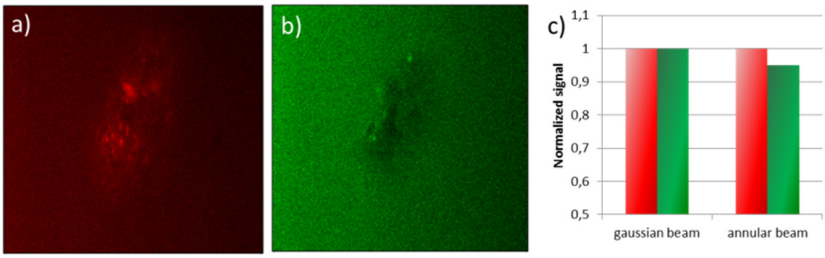

Figure 5.4. Images obtained from a sample phantom comprising fluorescein and red microspheres dissolved in agar, acquired using an experimental MPM set-up showing the same region in both channels. The red channel (a) shows the fluorescence from several micro-spheres in the focal plane, while the green channel (b) corresponds to the fluorescein signal, generated both in the focus as well as background. The bar chart (c) demonstrates the decrease in the signal of the green channel when switching from Gaussian to an annular beam. Field of view: ~200 x 200 µm.

5.1.2.2 SLM with scattering phantoms and skin (Paper IV)

One of the pattern used in the measurements performed is detailed in Figure 5.5, along with the corresponding beam profile. This was the pattern used in the measurements presented below. As can be seen, the annular beam is not perfect.

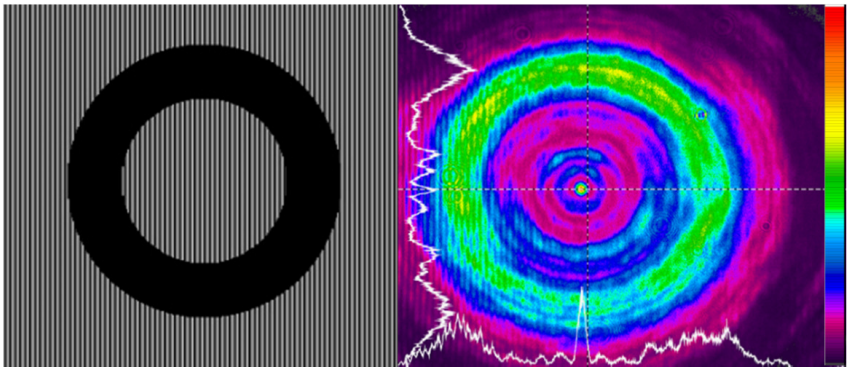

Figure 5.5. A pattern (left) sent to the SLM to produce an annular beam and the resulting intensity profile (right). The beam have a *b/B* ratio of approximately 0.4.

Experiments have been made on phantoms with an added scattering component, also described in Section 4.3.5, as well as on excised skin, as detailed in 4.3.5.3. Figure 5.6 shows the side-by-side comparison of MPM images of the fluorescent scattering phantom obtained using annular vs. Gaussian illumination with matching power (~15 mW at the back aperture) at ~450 µm sub-surface. The stained gauze fibers contribute to the signal in the red channel while the Fluorescein signal is seen in the gel surrounding the fibers in the green channel. As shown, the Gaussian images have prominent hazy background not present in the annular images.

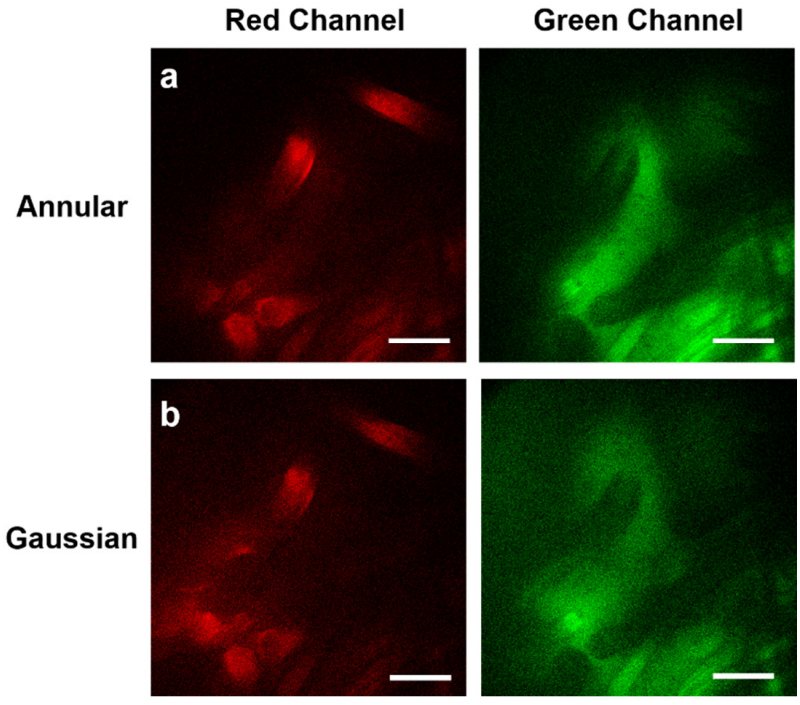

Figure 5.6. MPM images of a gel-based scattering fluorescent phantom using power-matched annular and Gaussian illumination at ~450µm sub-surface. The rhodamineB-ITC stained gauze fibers (fluorescent in the red channel) are embedded in a fluorescein stained agar gel (fluorescent in the green channel). Field of view ~250 x 250µm.

Figure 5.7 shows the side-by-side comparison of MPM images of an unstained excised human skin at two different depths within the dermis. The autofluorescence generated by the elastin and collagen from the dermis is clearly visualized. Some fluorescence can be observed in the red channel due to the inherent porphyrin content of the skin (not shown). At shallow depths with matching power (~20 mW at the back aperture), the imaging performance is comparable using annular and Gaussian illumination (Figure 5.7a). However, when imaging deeper into optically dense specimen, the imaging contrast is comparable for images obtained using annular illumination while the contrast is noticeably degraded by the overwhelming background in the images obtained with Gaussian illumination (Figure 5.7b).

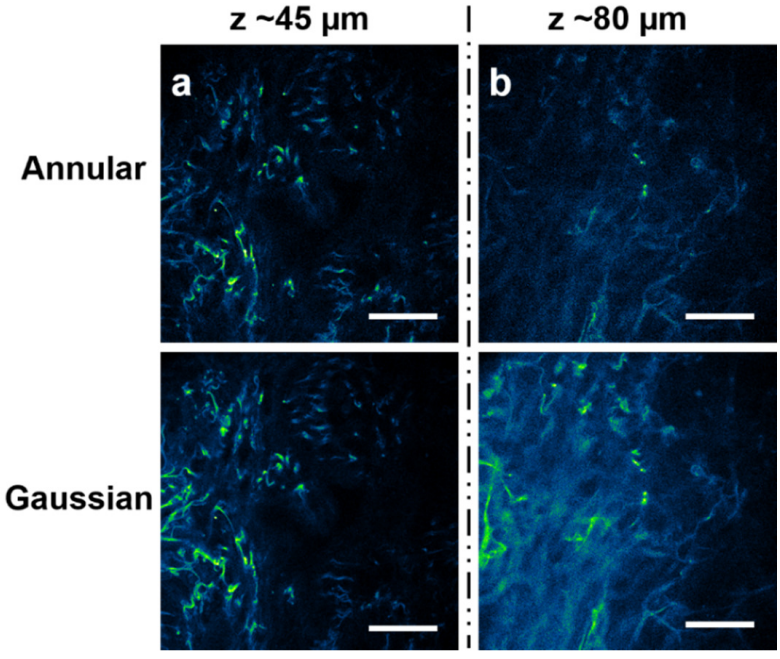

Figure 5.7. MPM images of an excised unstained normal human skin specimen. The autofluorescence generated by the elastin and collagen in the dermis can be clearly visualized at the depths of ~45µm (a) and ~80µm (b). The use of an annular beam reduces the uniform background which is present when imaging with a Gaussian beam. Scale bar = 50µm.

The reduction of the uniform background signal seen in this first proof-of-principle is minor but promising. These results show that it is possible to lower the out-of-focus fluorescence using annular illumination, and allow for deeper imaging into highly scattering tissue. Simulations, along with the work of Durr *et al.* [32], show the out-of-focus fluorescence increasing further at higher laser powers than are currently available in the experimental setup. A stronger excitation source might lead to data showing a larger improvement, and should be implemented.

5.2 Exploring AuNPs as contrast media (Paper II and III)

Gold nanoparticles, described in Chapter 2.6, 3.2 and 4.2 were used to explore MIL, and the MIL signal's dependency on the particle configuration (Paper II). Functionalized AuNPs were used to create a controllable contrast agent (Paper III).

5.2.1 Experiments on gradient plates

The aim of this study was to evaluate if gold nanospheres with a diameter of 10 nm would give rise to MIL in a mono-dispersed state, or if a degree of clustering is needed to detect the particles using multiphoton excitation.

A multiphoton mosaic image taken along the gradient, along with SEM images of the corresponding locations, can be found in Figure 5.8. The figure shows a clear correlation between clustering of particles in the far left end of the gradient and a high MIL signal. The middle region show a relatively low signal, despite a large concentration of (well-dispersed) AuNPs. A signal is seen from the far right, where some degree of clustering is present.

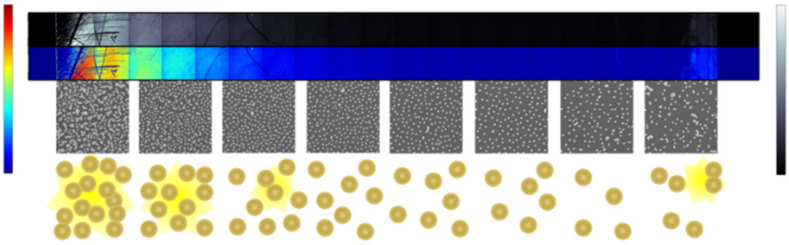

Figure 5.8. Emission images (560 – 680 nm) from an AuNP gradient plate consisting of chemically deposited spherical AuNPs (d = 10 nm) on a glass plate (size: 8.7 x 8.5 mm), acquired using MPM. A tile of 22 images scanned across the plate (field of view: 0.425 x 9.45 mm) is presented in both false color and grayscale (arbitrary units). All settings, i.e. excitation wavelength (740 nm), scan speed, gain, and offset were kept constant. SEM images are also included (field of view 545 x 545 µm), illustrating the particle distribution at different locations across the plate. Unintentional scratches in the AuNP layer on the plate surface are observed as irregular dark lines. The lower part of the image gives a schematic view of the particle distribution and interpretation of MIL generation.

From the AFM images shown in Figure 5.9, it could be concluded that the nanoparticles are predominantly deposited in a mono-layer. This implies that the SEM images provided by the plate manufacturers provides a good representation of the AuNP distribution.

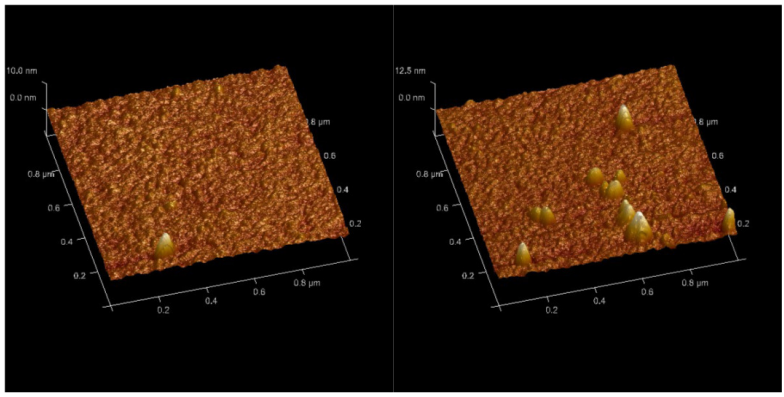

Figure 5.9. Image acquired using AFM on the a) sparse and b) nanoparticle-dense side of the gradient, showing that while a few vertical clusters exist, the majority of the particles are deposited in a mono-layer. This indicates that the SEM images provide a good indication of the particle coverage. Reprinted with permission from Paper II, supplementary materials.

The SEM images were used to extract the AuNP coverage along the gradient. The intensity measured along the gradient were then plotted against the AuNP coverage. The results, shown in Figure 5.10, clearly show a deviation from a linear relationship between the coverage and the signal, for coverages above 13%. This is the region in which AuNP clusters are present.

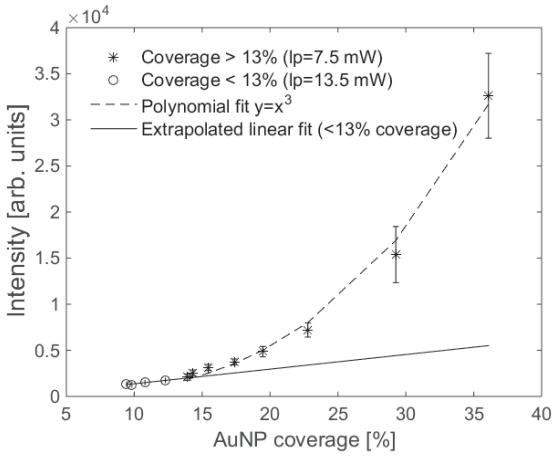

Figure 5.10. Analysis of the emission acquired from three substrates (n=3) as function of particle coverage. Maximum coverage measured from the SEM images was 37%. Laser power was increased from 7.5 mW to 13.5 mW (measured at back aperture of objective lens) to elevate signal from regions with low coverage (<13%). Included in the figure is a polynomial and a linear fit to demonstrate the deviation from linear dependency. Error bars show standard deviation.

By analyzing the slope value of the signal for different regions of the gradient, it was found that a high concentration of particles is not necessary to achieve MIL, as long as some particles are clustered. The slope values obtained from measurements along the gradient are shown in Figure 5.11. As can be seen, the slope value is consistently >2 for large clusters, indicating a non-linear process, *i.e.* MIL.

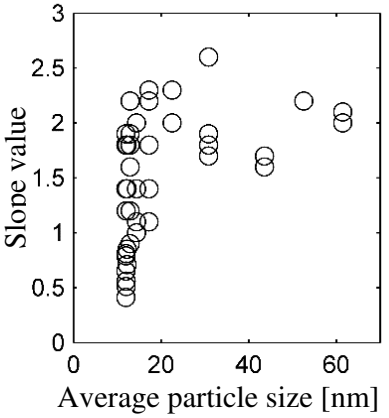

Figure 5.11. Results of the analysis of the MIL-signals dependency on cluster size. Measurements have been made along the gradient. The slope value, which indicates if the signal originates from a single or multiphoton process, show that the multiphoton process (a slope value of ~2) dominate for large clusters.

In addition, a decreasing emission signal similar to rapid bleaching was observed during the scanning of the plates. The intensity of the emission from the exposed area dropped to 30% of the original signal after exposure, and recovered to 90% of the original intensity after 3.5 hours. This is likely due to a combination of melting and photo-oxidation. The melting irreversibly destroys the structure of the sphere, while the photo-oxidation temporaily removes the electron cloud needed to absorb the excitation beam. The particles recover when they are reduced by the surrounding water.

We can conclude that the degree of clustering plays an important role in the generation of MIL in gold nanospheres, which provided grounds for our further exploration of the topic, further detailed in the next Section. As discussed in Section 3.2, the particles close proximity allows for new plasmon modes, which in turn allows for a higher intra-band transition rate $\sigma_{sp\rightarrow sp}$. This causes more holes in the *d*-band and an enhancement to the MIL signal.

5.2.2 Theoretical insights

The study revealed a clearer image of the process behind MIL. These new results are presented in Figure 5.12. The results expand upon the work by Imura *et al.* [109]. In particular, it provides an explanation for the relaxation processes involved in MIL. The nature of the process, together with the band structure of gold, explains why the efficiency of MIL depends on the absorption at the laser wavelength, and not at half the wavelength, which is the case for multi-photon excitation of fluorophores. This is motivated by Imura, using a polarization argument, and is here shown both theoretically and experimentally. The clustering of AuNPs red-shifts the absorption peak, which increases the absorption in the NIR range, where the absorptions explored here take place. These results are further detailed in Paper II.

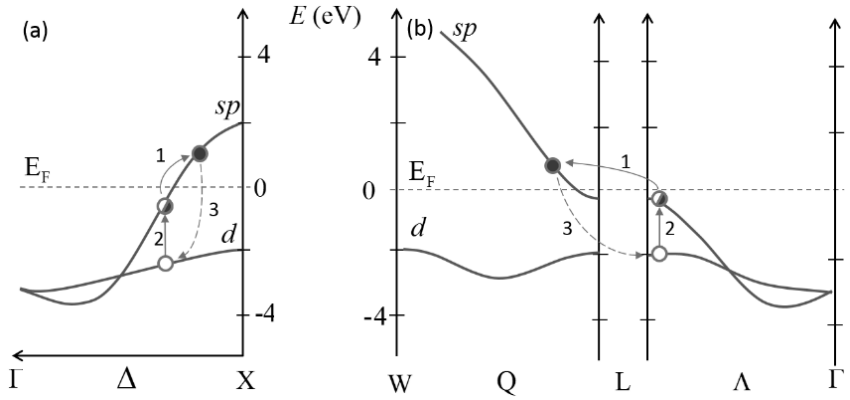

Figure 5.12. Schematic diagram of the electron transfers during MIL of AuNPs near the X (a) and L (b) symmetry points. Band structure was calculated by Eckardt *et al.* [131]. The process behind MIL is conceptually illustrated as a sequential absorption [109, 110] of two NIR photons (800 nm, approx. 1.5 eV). The absorption of the first photon (1) creates a hole below the Fermi-level through an intra-band indirect transition of a conducting electron within the *sp*-band. Through a subsequent photon (2) absorption, this whole is filled from the *d*-band. The luminescence is represented as an inter-band transition occurring when a *sp*-band electron refills the hole in the *d*-band. The bent arrows imply that electronic transitions are coupled to phonon excitations. The dashed arrow indicate that thermalization and scattering might precede transition [111, 115]. E_F indicates the Fermi surface. Used with permission from Paper II [132].

5.2.3 Functionalized gold nanoparticles

Further experiments were made in order to utilize the dependency of MIL on particle distance for imaging, using AuNPs functionalized with custom peptides. To evaluate the controlled, Zn^{2+}-mediated aggregation of the functionalized AuNPs, UV-Vis measurements were performed. The results can be seen in Figure 5.13. The graphs show a significant shift in the LSPR-peak, indicating an aggregation of the particles in the presence of Zn^{2+} [101]. The addition of EDTA to the solution reversed the aggregation and produced an absorption spectra identical in shape to that of the AuNPs before the addition of Zn^{2+} (data not shown).

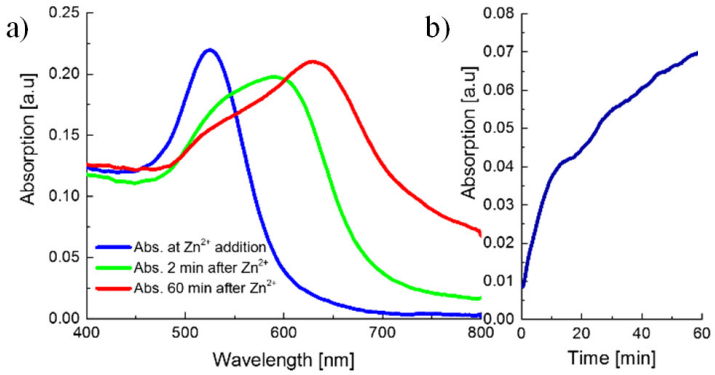

Figure 5.13. The effect of Zn^{2+} addition illustrated by a) absorption spectra taken before the addition of Zn^{2+}, 2 minutes after the addition and 60 minutes after the addition of Zn^{2+}, showing the shift in the LSPR peak, and b) the increased absorption at the laser wavelength (800 nm).

Multiphoton volume scans of the sets of solutions show a clear change in MIL signal from the mono-dispersed particles to the clusters. One such scan is shown in Figure 5.14. As can be seen in the figure, no distinguishable signal is seen for the mono-dispersed particles, while the clusters are clearly visible. This implies that the MIL signal heavily depends on particle configuration for 20 nm AuNPs.

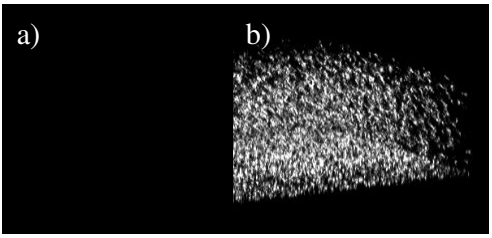

Figure 5.14. A representative image of a), monodispersed AuNPs and b) the same concentration of AuNPs, with added Zn^{2+} to facilitate the aggregation. A deposition of AuNPs clusters can be seen in the lower part of image b), indicating a sedimentation of the clusters. It is however clear from the image that sedimentation is not needed for a detectable signal. Field of view: 424 x 424 x 151 µm.

To evaluate the structure change during measurements, TEM was performed on the grid, and the resulting images (Figure 5.15) show a clear change in structure of the exposed nanoparticles. Initially, the internal structure is lost as the peptide binding the particles together is denatured. This causes closer clustering. Prolonged exposure causes the particles to melt together and form larger spheres. Both of these effects results in a particle system with a greater absorption in the NIR region, which in turn gives rise to a higher MIL signal.

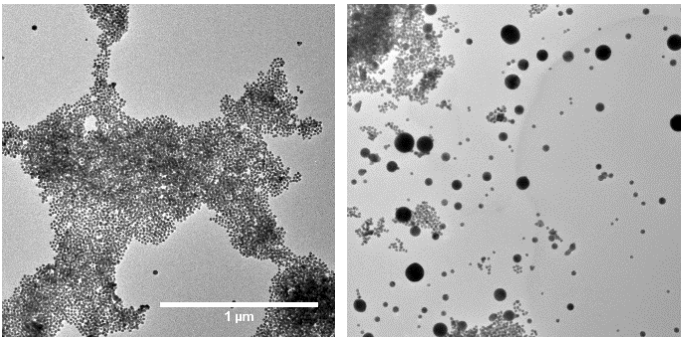

Figure 5.15. TEM of 20 nm AuNPs on a TEM grid. The particles have sedimented after aggregating in the presence of Zn^{2+}, due to their peptide functionalization. Repeated imaging of the right side of the grid exposes the particles sedimented here to energy levels high enough to change their properties. Images of the TEM-grid show physical changes in the exposed particles, indicating smaller inter-particle distances, and more evidently, the combination of smaller particles into bigger particles (diameter approximately 100 nm) through melting. Field of view: 2.1 x 2.1 µm at 9500x magnification. Scale bar: 1 µm.

These results stand in contrast to the results obtained using gradient plates, where a bleaching was seen. This is most likely due to the fact that the particles remained fixed on the gradient plates, and could not cluster further, while the functionalized particles could form larger clusters during exposure, and thus increase their absorption further.

5.3 Implementation of experimental imaging system

The experimental imaging system designed for the purpose of evaluating annular beams in MPM has the potential of being used for a multitude of purposes. Some examples of initial studies are presented here.

5.3.1 Multiphoton FLIM

The TCSPC capabilities of the system allows for multiphoton FLIM imaging, in which an additional dimension is added to the image through the recording and calculation of the decay times of the different fluorophores. An example of such an image is shown in Figure 5.16. The image shows a projection of images taken in a skin sample. Clear differences in decay times can be seen.

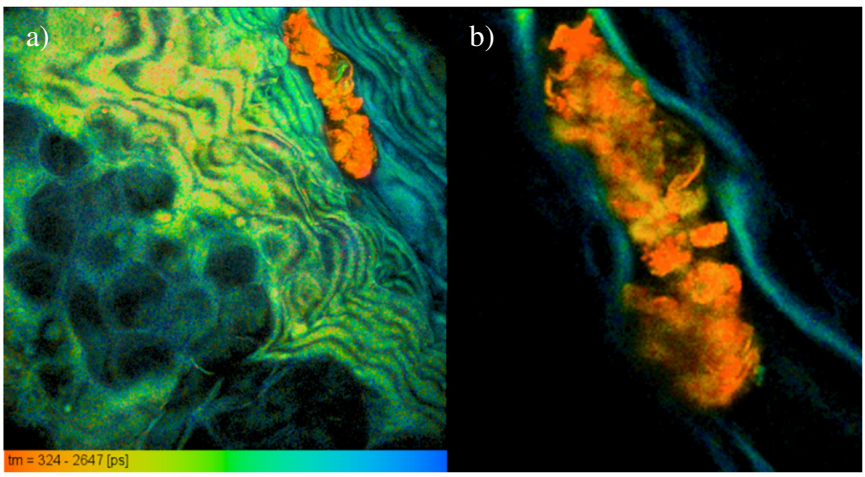

Figure 5.16. a) the sum of a stack of images taken of superficial skin cells. Different decay times, represented by color, can be seen for different parts of the skin. b) shows a magnification of one of the images, showing a possible *Dermodex* (skin mite). Image made using Becker&Hickl software. Field of view for full image: 250x250 µm.

5.3.2 Imaging of biofilms

So far, the primary application of the system, outside the experiments detailed so far in this thesis, has been the imaging of biofilms, as part of the EU-project Cyclon-HIT to study anti-microbial resistance. The biofilms were stained with SYTO 9/PI and imaged after two days. Resulting images are shown in Figure 5.17. As shown in the image, biofilms can be visualized using the setup, allowing tracking of growth and decay of whole films. An on-stage incubator (Ibidis 10918), including temperature, CO_2, and flow control, has recently been installed to allow for continuous monitoring of biofilm growth for future longitudinal studies.

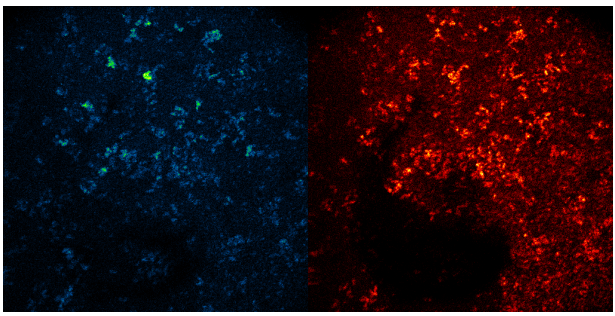

Figure 5.17. Biofilms of bacteria imaged using the experimental setup. The bacteria are live/dead stained using SYTO 9/PI, with live cells in the left channel and dead in the right. Approximate field of view: 1000 x 1000 µm.

5.3.3 Controlled photo-activation

By using the automated stage, samples were exposed to laser radiation in a controlled pattern. This will eventually be used for photo-activation experiments, where whole bio-films will be exposed and then imaged, both using the experimental system. The patterns were evaluated using stained microscope slides, which bleaches when exposed to strong laser light. An image of such a slide, bleached in a pattern, is shown in Figure 5.18, where dark squares can be seen. These squares correspond to areas where the slide has been exposed.

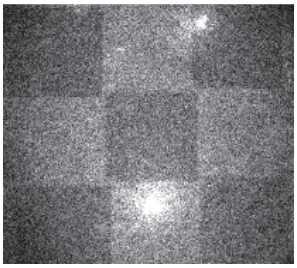

Figure 5.18. A photo-bleached microscopy slide, showing a pattern achieved by moving the stage after each exposure. This allows the system to perform photo-activation of cells in a controlled manner. Approximate field of view: 1000 x 1000 µm.

An experimental system is ideal for integrating novel methods into an already functioning microscope setup, and work is ongoing to further utilize this asset.

6 Discussion & Conclusions

In this thesis, I have explored a methodology based on introducing annular shaped laser beam in MPM with the aim to reduce out-of-focus generated background signal and increase imaging depth. I have also shown how spherical AuNPs can be utilized as controllable contrast media based on MIL, by changing the inter-particle distance.

Mathematical models of annular beams were constructed, showing that 40% of the beam radius can be blocked while preserving an acceptable axial resolution. The technique was implemented in an experimental system using a beam-blocker and, later, a SLM to modulate the beam. Acquired results, primarily in tissue phantoms, but also in excised tissue, show that the technique can be used to reduce out-of-focus fluorescence. Further experiments are under way to quantify this effect, using higher laser powers and a more precise control of the laser beam. A higher laser power will result in a higher fluorescence generation at the sample surface. This should make the effects of annular beams clearer, and allow imaging even further into skin samples. A greater imaging depth will allow non-invasive imaging of previously unreachable cell layers, which is essential for the understanding of the processes behind e.g. malignant melanoma. A goal of the work detailed in this thesis has been to investigate if annular beams can be used to increase imaging depth in biological tissue. Results indicate that this is the case. However; the effect has yet to be fully quantified, along with the parameters which determines its efficiency.

The experiments performed on spherical 10-20 nm AuNPs highlighted the large dependency of MIL on cluster size and internal configuration. It was found that MIL was only detectable from clusters of at least two particles, and for inter-particle distances of one particle diameter or below. This was used to implement a switchable contrast agent for MPM, by using AuNPs with controllable aggregation. This not only shows the potential of the two techniques combined, but also provides a way to sense *e.g.* pH and ion concentration changes using non-invasive microscopy. Access to better contrast agents is desired within the field of microscopy, and the successes of the PALM

technique, which builds upon a different approach to switchable contrast agents, show the importance of dynamic contrast media. In theory, the system could be used to build a contrast agent inside a sample, by letting dispersed particles diffuse in, and subsequently aggregating the particles.

A main focus of this thesis is the design and development of a customized MPM. The setup comprises optical elements and data acquisition using custom and commercially available software. This experimental platform will allow the research group to further explore non-linear optics through modifications of the optical path, i.e. the implementation of annular beams.

The work presented in this thesis has resulted in several findings of importance. New applications of annular beams has been explored, as well as new ways of generating and evaluating said beams. The available knowledge of MIL has been expanded upon with further experiments. These experiments not only confirm the underlying processes behind MIL, but also highlight the possible applications of AuNPs in MPM.

In conclusion, by exploring novel ways to enhance imaging contrast in MPM for medical imaging, new techniques have been established to enhance the performance of not only MPM, but of laser scanning microscopes in general.

7 Outlook

The projects presented here by no means conclude the development of MPM. Rather, they serve as stepping stones for future developments, with potential implications for other laser scanning microscopy techniques.

For the experimental setup, the work carried out by Durr *et al.* [32] indicates that the technique should be more efficient at higher laser powers than the 800 mW currently available in the system. Optimizing the optics and using a more powerful laser could show a more significant improvement. Care should be taken to avoid damage on the SLM from to high intensities. With a higher excitation power, the imaging depth can potentially be extended to the levels where models show a greater impact of the modifications to the laser beam.

Every optical element in the optical path adds a bit of dispersion to the laser pulse. As the technique relies on a pulse which is narrow in the time domain, this effect will degrade image quality. The dispersion can be measured and quantified with an auto-correlator. An easy modification to lower the dispersion is to replace the wave-plate with a set of two mirrors which also turns the polarization 90°. The dispersion can also be compensated for with the introduction of a pulse-compressor. More experiments should be made to further quantify the effect, and several more SLM patterns should be calculated and evaluated. Preferably, this would be done using the beam profiler for direct digital feedback.

The AuNPs show potential as a contrast agent, but so far, the measurements have only been done in solution. The concept should be tried in a more complex sample, where conditions are inhomogeneous, to evaluate the practical functionality of the system. Preferably, a biological sample should be used to highlight the potential of the approach. A sample which undergoes changes in pH should be explored, to evaluate the particles potency as a pH-indicator, as described by Aili *et al.* [122]. The experiments done proves that AuNPs can be used as controllable contrast agents. This result holds true for similar systems of AuNPs, functionalized to aggregate under different conditions, which should also be explored.

Annular beams and switchable contrast both offer new possibilities to the field of MPM. More importantly, they do so in parallel with other techniques currently in development, such as optical clearing [133] and three-photon microscopy [134]. The knowledge gained here about the processes involved when using annular beams could easily be implemented together with other methods to improve MPM, even those which already uses beam modulation. A successful implementation of annular beams will allow for greater imaging depths, possibly reaching new cell layers in skin, as well as the important layer V neurons in the human brain, which will prove valuable for medical research.

The approach of controlling MIL through aggregation could also be used together with many of the advanced microscopy techniques available today. It has the potential to allow non-invasive read-out of nanoparticle sensors, as well as increased image quality through switchable contrast.

8 Acknowledgements

I would like to thank my advisor Marica Ericson for taking me in and guiding me from a student to a researcher, and for remaining positive and optimistic whatever happens. I think we make a great team, and this thesis would not have been possible without you!

Many thanks to my examiner Dag Hanstorp, who has been of great help with his theoretical knowledge, gadgets, feedback and general advice and encouragements! Your attention for detail is amazing!

Thanks to Ingvar Albinsson for being co-supervisor and providing valuable LabVIEW support!

Many thanks to the past and present members of the Biomedical Photonics Group! (Hanna Thomsen, Joakim Zaar, Vladimir Kirejev, Stina Guldbrand, Brigitte Bauer, Melina Möchel, Friederike Geerken, Thomas Guttenberg, Yuanmo Wang, and Olle Bergel). It has truly been my pleasure working with you! Thanks to Daniel Aili and Robert Selegård for letting me use your particles, and for being amazing to write articles with! The paper is golden! Thanks to Hanne Evenbratt for your help and positive attitude, and to Oscar Isaksson for being a nice and understanding lab-mate. Thanks to Nicholas Durr, Onur Ferhanoglu, Ann-Marie Wennberg, Timur Shegai, Adela Ben-Yakar and the people of SkinResQu and Cline Scientific AB for providing valuable input to my work!

Thanks to Maria Smedh, Julia Fernandez-Rodriguez, and the others at the center for cellular imaging at Sahlgrenska for giving me hands-on experience with microscopes, as well as support. To Laser-Patrik Frihlén for being very helpful, and for finding the last controller card in the world for me, and to Martin Sveningsson for valuable programming lessons! Thanks to the people in the mechanical workshop for practical solutions to complex problems!

I would also like to thank all the people on Physics level 8 and Chemistry level 9/8, especially the Dermatochemistry group for all the nice discussions over coffee in the lunch room! Especially to David Ponting for being a fun person, and to Sebastian Kaminski for eating

all the buns so I didn't have to. To Johanna Gustavsson, Maria Siirak and Helena Bergkvist for dealing with my sometimes quite complex employment status at Physics and Chemistry, and all the other ever helpful administrators as well of course!

Thanks to the faculty of science at Gothenburg University, Vetenskapsrådet and Lundbergsstiftelsen for financing this research, and to Adlerbertska Stiftelsen, Sixten Gemzéus stiftelse, Sahlgrenska Universitetssjukhuset and Kungl och Hvitfeldtska stiftelsen for making my travels around the world possible.

Thanks to Veraspexet for providing me with social interactions and lots of fun work outside of work! To Ida, and all my other friends around the world, for being there and remembering me when I forget.

The biggest of thanks to my family, for the infinite support, love and LEGO-sets. To my grand-parents, for inspiring me to study biomedical engineering, as well as providing love and shelter whenever needed. I wish I could have shared this with all of you.

My biggest thanks to Danni. You are still the best thing I have found while doing research. Cat!

9 Bibliography

1. Nie, S., D. Chiu, and R. Zare, *Probing individual molecules with confocal fluorescence microscopy.* Science, 1994. **266**(5187): p. 1018-1021.
2. Guldbrand, S., et al., *Two-photon fluorescence correlation spectroscopy as a tool for measuring molecular diffusion within human skin.* European Journal of Pharmaceutics and Biopharmaceutics, 2013. **84**(2): p. 430-436.
3. Hell, S.W. and J. Wichmann, *Breaking the diffraction resolution limit by stimulated emission: stimulated-emission-depletion fluorescence microscopy.* Optics Letters, 1994. **19**(11): p. 780-782.
4. Hess, S.T., T.P.K. Girirajan, and M.D. Mason, *Ultra-High Resolution Imaging by Fluorescence Photoactivation Localization Microscopy.* Biophysical Journal, 2006. **91**(11): p. 4258-4272.
5. Hell, S.W., *Microscopy and its focal switch.* Nat Meth, 2009. **6**(1): p. 24-32.
6. Betzig, E., et al., *Imaging intracellular fluorescent proteins at nanometer resolution.* Science, 2006. **313**(5793): p. 1642-1645.
7. Göppert-Mayer, M., *Über Elementarakte mit zwei Quantensprüngen.* Annalen der Physik, 1931. **401**(3): p. 273-294.
8. Denk, W., J. Strickler, and W. Webb, *Two-photon laser scanning fluorescence microscopy.* Science, 1990. **248**(4951): p. 73-76.
9. So, P.T.C., et al., *TWO-PHOTON EXCITATION FLUORESCENCE MICROSCOPY.* Annual Review of Biomedical Engineering, 2000. **2**(1): p. 399-429.
10. König, K., *Clinical multiphoton tomography.* Journal of Biophotonics, 2008. **1**(1): p. 13-23.
11. Rajadhyaksha, M., R.R. Anderson, and R.H. Webb, *Video-rate confocal scanning laser microscope for imaging human tissues in vivo.* Applied Optics, 1999. **38**(10): p. 2105-2115.
12. Busam, K.J., et al., *Detection of clinically amelanotic malignant melanoma and assessment of its margins by in*

vivo confocal scanning laser microscopy. Arch Dermatol, 2001. **137**(7): p. 923-9.

13. Evenbratt, H., et al., *In vivo study of an instantly formed lipid-water cubic phase formulation for efficient topical delivery of aminolevulinic acid and methyl-aminolevulinate.* Int J Pharm, 2013. **452**(1-2): p. 270-5.
14. Kantere, D., et al., *Anti-Stokes fluorescence from endogenously formed protoporphyrin IX - Implications for clinical multiphoton diagnostics.* Journal of Biophotonics, 2013. **6**(5): p. 409-415.
15. Paoli, J., et al., *Multiphoton laser scanning microscopy on non-melanoma skin cancer: morphologic features for future non-invasive diagnostics.* J Invest Dermatol, 2008. **128**(5): p. 1248-55.
16. Paoli, J., M. Smedh, and M.B. Ericson, *Multiphoton Laser Scanning Microscopy-A Novel Diagnostic Method for Superficial Skin Cancers.* Seminars In Cutaneous Medicine And Surgery, 2009. **28**(3): p. 190-195.
17. Ericson, M.B., et al., *Two-photon laser-scanning fluorescence microscopy applied for studies of human skin.* J Biophotonics, 2008. **1**(4): p. 320-30.
18. Sandberg, C., et al., *Fluorescence Diagnostics of Basal Cell Carcinomas Comparing Methyl-aminolaevulinate and Aminolaevulinic Acid and Correlation with Visual Clinical Tumour Size.* Acta Dermato-Venereologica, 2011. **91**(4): p. 398-403.
19. Roberts, M.S., et al., *Non-invasive imaging of skin physiology and percutaneous penetration using fluorescence spectral and lifetime imaging with multiphoton and confocal microscopy.* Eur J Pharm Biopharm, 2011. **77**(3): p. 469-88.
20. Seidenari, S., et al., *Multiphoton laser microscopy and fluorescence lifetime imaging for the evaluation of the skin.* Dermatol Res Pract, 2012. **2012**: p. 810749.
21. Gonzalez, S., M. Rajadhyaksha, and R.R. Anderson, *Non-invasive (real-time) imaging of histologic margin of a proliferative skin lesion in vivo.* J Invest Dermatol, 1998. **111**(3): p. 538-9.
22. Rajadhyaksha, M., et al., *In vivo confocal scanning laser microscopy of human skin II: advances in instrumentation*

and comparison with histology. J Invest Dermatol, 1999. **113**(3): p. 293-303.

23. Larson, B., et al., *Detection of skin cancer margins in Mohs excisions with high-speed strip mosaicing confocal microscopy: A feasibility study.* British Journal of Dermatology, 2013. **169**(4): p. 922-926.
24. Zipfel, W.R., R.M. Williams, and W.W. Webb, *Nonlinear magic: multiphoton microscopy in the biosciences.* Nat Biotech, 2003. **21**(11): p. 1369-1377.
25. Ericson, M.B., et al., *Two-photon laser-scanning fluorescence microscopy applied for studies of human skin.* Journal of Biophotonics, 2008. **1**(4): p. 320-330.
26. Masters, B.R., P.T.C. So, and E. Gratton, *Multiphoton excitation fluorescence microscopy and spectroscopy of in vivo human skin.* Biophysical Journal, 1997. **72**(6): p. 2405-2412.
27. König, K., *Multiphoton microscopy in life sciences.* Journal of Microscopy, 2000. **200**(2): p. 83-104.
28. Guldbrand, S., et al., *Two-photon fluorescence correlation microscopy combined with measurements of point spread function; investigations made in human skin.* Optics Express, 2010. **18**(15): p. 15289-15302.
29. Diaspro, A., G. Chirico, and M. Collini, *Two-photon fluorescence excitation and related techniques in biological microscopy.* Quarterly Reviews of Biophysics, 2005. **38**(02): p. 97-166.
30. Bender, J., et al., *Lipid cubic phases in topical drug delivery: Visualization of skin distribution using two-photon microscopy.* Journal of Controlled Release, 2008. **129**(3): p. 163-169.
31. Helmchen, F. and W. Denk, *Deep tissue two-photon microscopy.* Nature Methods, 2005. **2**(12): p. 932-940.
32. Durr, N.J., et al., *Maximum imaging depth of two-photon autofluorescence microscopy in epithelial tissues.* Journal of Biomedical Optics, 2011. **16**(2): p. 026008.
33. Sperling, R.A., et al., *Biological applications of gold nanoparticles.* Chemical Society Reviews, 2008. **37**: p. 13.

34. Ghosh, P., et al., *Gold nanoparticles in delivery applications.* Advanced Drug Delivery Reviews, 2008. **60**(11): p. 1307-1315.
35. Huang, X., et al., *Gold nanoparticles: Interesting optical properties and recent applications in cancer diagnostics and therapy.* Nanomedicine, 2007. **2**(5): p. 681-693.
36. Murphy, C.J., et al., *Gold Nanoparticles in Biology: Beyond Toxicity to Cellular Imaging.* Accounts of Chemical Research, 2008. **41**(12): p. 1721-1730.
37. Park, J., et al., *Two-photon-induced photoluminescence imaging of tumors using near-infrared excited gold nanoshells.* Optics Express, 2008. **16**(3): p. 10.
38. Durr, N.J., et al., *Two-Photon Luminescence Imaging of Cancer Cells Using Molecularly Targeted Gold Nanorods.* Nano Letters, 2007. **7**(4): p. 941-945.
39. Connor, E.E., et al., *Gold nanoparticles are taken up by human cells but do not cause acute cytotoxicity.* Small, 2005. **1**(3): p. 325-327.
40. Hell, S.W., et al., *Annular aperture two-photon excitation microscopy.* Optics Communications, 1995. **117**(1–2): p. 20-24.
41. Sheppard, C.J.R. and T. Wilson, *Imaging properties of annular lenses.* Appl. Opt., 1979. **18**(22): p. 3764-3769.
42. Sheppard, C.J. and A. Choudhury, *Annular pupils, radial polarization, and superresolution.* Applied optics, 2004. **43**(22): p. 4322-4327.
43. Hecht, E., *Optics*. 2002: Addison-Wesley.
44. Croft, W.J., *Under the Microscope: A Brief History of Microscopy*. 2006: World Scientific.
45. Dobell, C. and A.v. Leeuwenhoek, *Antony van Leeuwenhoek and his "Little animals"; being some account of the father of protozoology and bacteriology and his multifarious discoveries in these disciplines; collected, translated, and edited from his printed works, unpublished manuscripts, and contemporary records, by Clifford Dobell ... Published on the 300th anniversary of his birth*. 1932, New York: Harcourt, Brace and company.
46. Bertolotti, M., *The history of the laser*. 2004: CRC press.

47. Amos, W.B. and J.G. White, *How the confocal laser scanning microscope entered biological research.* Biology of the Cell, 2003. **95**(6): p. 335-342.
48. White, J.G., W.B. Amos, and M. Fordham, *An evaluation of confocal versus conventional imaging of biological structures by fluorescence light microscopy.* Journal of Cell Biology, 1987. **105**(1): p. 41-48.
49. Minsky, M., *Microscopy apparatus*. 1961, Google Patents.
50. Paddock, S., *Over the rainbow: 25 years of confocal imaging.* Biotechniques, 2008. **44**(5): p. 643-4, 646, 648.
51. Shotton, D.M., *Confocal scanning optical microscopy and its applications for biological specimens.* Journal of Cell Science, 1989. **94**(2): p. 175-206.
52. König, K., et al., *Clinical two-photon microendoscopy.* Microscopy Research and Technique, 2007. **70**(5): p. 398-402.
53. Kirejev, V., et al., *Multiphoton microscopy - A powerful tool in skin research and topical drug delivery science.* Journal of Drug Delivery Science and Technology, 2012. **22**(3): p. 250-259.
54. Pinkel, D., T. Straume, and J. Gray, *Cytogenetic analysis using quantitative, high-sensitivity, fluorescence hybridization.* Proceedings of the National Academy of Sciences, 1986. **83**(9): p. 2934-2938.
55. Pierce, M.C., D.J. Javier, and R. Richards-Kortum, *Optical contrast agents and imaging systems for detection and diagnosis of cancer.* International Journal of Cancer, 2008. **123**(9): p. 1979-1990.
56. Masters, B.R., P.T. So, and E. Gratton, *Multiphoton excitation fluorescence microscopy and spectroscopy of in vivo human skin.* Biophysical Journal, 1997. **72**(6): p. 2405-2412.
57. Xu, C., et al., *Multiphoton fluorescence excitation: New spectral windows for biological nonlinear microscopy.* Proceedings of the National Academy of Sciences of the United States of America, 1996. **93**(20): p. 10763-10768.
58. Centonze, V.E. and J.G. White, *Multiphoton Excitation Provides Optical Sections from Deeper within Scattering*

Specimens than Confocal Imaging. Biophysical Journal, 1998. **75**(4): p. 2015-2024.

59. Skala, M.C., et al., *In vivo multiphoton microscopy of NADH and FAD redox states, fluorescence lifetimes, and cellular morphology in precancerous epithelia.* Proceedings of the National Academy of Sciences, 2007. **104**(49): p. 19494-19499.
60. Phan, T.G. and A. Bullen, *Practical intravital two-photon microscopy for immunological research: faster, brighter, deeper.* Immunol Cell Biol, 2010. **88**(4): p. 438-444.
61. Joshi, B.P. and T.D. Wang, *Exogenous Molecular Probes for Targeted Imaging in Cancer: Focus on Multi-modal Imaging.* Cancers (Basel), 2010. **2**(2): p. 1251-87.
62. Koenig, K. and I. Riemann, *High-resolution multiphoton tomography of human skin with subcellular spatial resolution and picosecond time resolution.* Journal of Biomedical Optics, 2003. **8**(3): p. 432-439.
63. Stenquist, B., et al., *Bispectral fluorescence imaging of aggressive basal cell carcinoma combined with histopathological mapping: a preliminary study indicating a possible adjunct to Mohs micrographic surgery.* British Journal of Dermatology, 2006. **154**(2): p. 305-309.
64. König, K., et al., *Cellular response to near-infrared femtosecond laser pulses in two-photon microscopes.* Optics Letters, 1997. **22**(2): p. 135-136.
65. Frostig, R., *In vivo optical imaging of brain function*. 2002: CRC Press.
66. Richards, B. and E. Wolf, *Electromagnetic Diffraction in Optical Systems. II. Structure of the Image Field in an Aplanatic System.* Proceedings of the Royal Society of London A: Mathematical, Physical and Engineering Sciences, 1959. **253**(1274): p. 358-379.
67. Theer, P. and W. Denk, *On the fundamental imaging-depth limit in two-photon microscopy.* Journal of the Optical Society of America A, 2006. **23**(12): p. 3139-3149.
68. Herold, K.E. and A. Rasooly, *Biosensors and molecular technologies for cancer diagnostics*. 2012: CRC Press.

69. Becker, W., *Fluorescence lifetime imaging – techniques and applications.* Journal of Microscopy, 2012. **247**(2): p. 119-136.
70. Read, I.A. and V. David. *New developments in ultrafast lasers for biological applications*. 2006.
71. John, D., *Pockels cell*. 'Oxford University Press'.
72. Igasaki, Y., et al., *High Efficiency Electrically-Addressable Phase-Only Spatial Light Modulator.* Optical Review. **6**(4): p. 339-344.
73. Reicherter, M., et al., *Optical particle trapping with computer-generated holograms written on a liquid-crystal display.* Optics Letters, 1999. **24**(9): p. 608-610.
74. Hornbeck, L.J., *Spatial light modulator and method*. 1987, Google Patents.
75. Maurer, C., et al., *What spatial light modulators can do for optical microscopy.* Laser & Photonics Reviews, 2011. **5**(1): p. 81-101.
76. Lakowicz, J.R., *Principles of Fluorescence Spectroscopy*. 2007: Springer.
77. Elson, D.S., et al., *Real-time time-domain fluorescence lifetime imaging including single-shot acquisition with a segmented optical image intensifier.* New Journal of Physics, 2004. **6**(1): p. 180.
78. Sanchez, W., et al., *Fluorescence Lifetime Imaging of the Skin*, in *Advanced Time-Correlated Single Photon Counting Applications*, W. Becker, Editor. 2015, Springer International Publishing. p. 457-508.
79. Suhling, K., P.M.W. French, and D. Phillips, *Time-resolved fluorescence microscopy.* Photochemical and Photobiological Sciences, 2005. **4**(1): p. 13-22.
80. Yeh, S.C., et al., *Monitoring photosensitizer uptake using two photon fluorescence lifetime imaging microscopy.* Theranostics, 2012. **2**(9): p. 817-26.
81. Kirejev, V., et al., *Photophysics and ex vivo biodistribution of β-cyclodextrin-meso- tetra(m-hydroxyphenyl)porphyrin conjugate for biomedical applications.* Photochemical and Photobiological Sciences, 2014. **13**(8): p. 1185-1191.

82. Tiwari, P.M., et al., *Functionalized gold nanoparticles and their biomedical applications.* Nanomaterials, 2011. **1**(1): p. 31-63.
83. Sokolov, K., et al., *Real-Time Vital Optical Imaging of Precancer Using Anti-Epidermal Growth Factor Receptor Antibodies Conjugated to Gold Nanoparticles.* Cancer Research, 2003. **63**(9): p. 1999-2004.
84. Faulk, W.P. and G.M. Taylor, *An immunocolloid method for the electron microscope.* Immunochemistry, 1971. **8**: p. 3.
85. Hermann, R., P. Walther, and M. Müller, *Immunogold labeling in scanning electron microscopy.* Histochemistry and Cell Biology, 1996. **106**(1): p. 9.
86. Cognet, L., et al., *Single metallic nanoparticle imaging for protein detection in cells.* Proceedings of the National Academy of Sciences, 2003. **100**(20): p. 11350-11355.
87. Daniel, M.-C. and D. Astruc, *Gold Nanoparticles: Assembly, Supramolecular Chemistry, Quantum-Sized Related Properties, and Applications toward Biology, Catalysis, and Nanotechnology.* Chemical Reviews, 2004. **104**: p. 54.
88. Chen, D.-R., C.H. Wendt, and D.Y.H. Pui, *A novel approach for introducing bio-materials into cells.* Journal of Nanoparticle Research, 2000. **2**: p. 7.
89. Chen, J., et al., *Gold Nanocages: Engineering Their Structure for Biomedical Applications.* Advanced Materials, 2005. **17**: p. 7.
90. Huang, X., et al., *Cancer Cell Imaging and Photothermal Therapy in the Near-Infrared Region by Using Gold Nanorods.* Journal of the American Chemical Society, 2006. **128**: p. 6.
91. Pissuwan, D., S.M. Valenzuela, and M.B. Cortie, *Therapeutic possibilites of plasmonically heated gold nanoparticles.* Trends in Biotechnology, 2006. **24**(2): p. 6.
92. Willets, K.A. and R.P. Van Duyne, *Localized Surface Plasmon Resonance Spectroscopy and Sensing.* Annual Review of Physical Chemistry, 2007. **58**(1): p. 267-297.
93. Ghosh, S.K. and T. Pal, *Interparticle Coupling Effect on the Surface Plasmon Resonance of Gold Nanoparticles: From Theory to Applications.* Chemical Reviews, 2007. **107**(11): p. 4797-4862.

94. Jennings, T. and G. Strouse, *Past, Present, and Future of Gold Nanoparticles*, in *Bio-Applications of Nanoparticles*, W.C.W. Chan, Editor. 2007, Springer New York: New York, NY. p. 34-47.
95. Sperling, R.A. and W.J. Parak, *Surface modification, functionalization and bioconjugation of colloidal inorganic nanoparticles.* Philosophical Transactions of the Royal Society of London A: Mathematical, Physical and Engineering Sciences, 2010. **368**(1915): p. 1333-1383.
96. Gao, J., et al., *Colloidal Stability of Gold Nanoparticles Modified with Thiol Compounds: Bioconjugation and Application in Cancer Cell Imaging.* Langmuir, 2012. **28**(9): p. 4464-4471.
97. Goldberg, M.W. and J. Fiserova, *Immunogold Labelling for Scanning Electron Microscopy*, in *Immunoelectron Microscopy: Methods and Protocols*, D.S. Schwartzbach and T. Osafune, Editors. 2010, Humana Press: Totowa, NJ. p. 297-313.
98. Rechberger, W., et al., *Optical properties of two interacting gold nanoparticles.* Optics Communications, 2003. **220**(1–3): p. 137-141.
99. Sonnichsen, C., et al., *A molecular ruler based on plasmon coupling of single gold and silver nanoparticles.* Nat Biotech, 2005. **23**(6): p. 741-745.
100. Sun, Y. and Y. Xia, *Increased sensitivity of surface plasmon resonance of gold nanoshells compared to that of gold solid colloids in response to environmental changes.* Analytical Chemistry, 2002. **74**(20): p. 5297-5305.
101. He, Y.Q., et al., *A study on the sizes and concentrations of gold nanoparticles by spectra of absorption, resonance Rayleigh scattering and resonance non-linear scattering.* Spectrochimica Acta Part A: Molecular and Biomolecular Spectroscopy, 2005. **61**(13–14): p. 2861-2866.
102. Haiss, W., et al., *Determination of Size and Concentration of Gold Nanoparticles from UV-VIS Spectra.* Analytical Chemistry, 2007. **79**: p. 7.
103. Boyd, G.T., Z.H. Yu, and Y.R. Shen, *Photoinduced luminescence from the noble metals and its enhancement on roughened surfaces.* Physical Review B, 1986. **33**(12): p. 14.

104. Stockman, M.I., et al., *Dependence of the multiphoton luminescence spectrum of single gold nanoparticles on the refractive index of the surrounding medium.* 2008. **7032**: p. 70321T-70321T-9.
105. Beversluis, M., A. Bouhelier, and L. Novotny, *Continuum generation from single gold nanostructures through near-field mediated intraband transitions.* Physical Review B, 2003. **68**: p. 10.
106. Botcherby, E.J., R. Juškaitis, and T. Wilson, *Scanning two photon fluorescence microscopy with extended depth of field.* Optics Communications, 2006. **268**(2): p. 253-260.
107. Planchon, T.A., et al., *Rapid three-dimensional isotropic imaging of living cells using Bessel beam plane illumination.* Nat Meth, 2011. **8**(5): p. 417-423.
108. Liu, Y., P. He, and D. Cline. *Vacuum laser acceleration tests*. in *Particle Accelerator Conference, 1999. Proceedings of the 1999*. 1999.
109. Imura, K., T. Nagahara, and H. Okamoto, *Near-Field Two-Photon-Induced Photoluminescence from Single Gold Nanorods and Imaging of Plasmon Modes.* Journal of Physical Chemistry B, 2005. **109**: p. 7.
110. Biagioni, P., et al., *Dynamics of Four-Photon Photoluminescence in Gold Nanoantennas.* Nano Letters, 2012. **12**(6): p. 2941-2947.
111. Mooradian, A., *Photoluminescence of metals.* Physical Review Letters, 1969. **22**(5): p. 185-187.
112. Ruosch, M., *Multiphoton Excited Luminescence of Gold Nanoparticles*. 2010.
113. Slablab, A., et al., *Second-harmonic generation from coupled plasmon modes in a single dimer of gold nanospheres.* Optics Express, 2011. **20**(1): p. 8.
114. Nah, S., L. Li, and J.T. Fourkas, *Field-Enhanced Phenomena of Gold Nanoparticles†.* The Journal of Physical Chemistry A, 2009. **113**(16): p. 4416-4422.
115. Biagioni, P., et al., *Dependence of the two-photon photoluminescence yield of gold nanostructures on the laser pulse duration.* Physical Review B, 2009. **80**(4).

116. Wang, H., et al., *In vitro and in vivo Two-Photon Luminescence Imaging of Single Gold Nanorods.* PNAS, 2005. **102**(44): p. 6.
117. Meglinski, I.V. and S.J. Matcher, *Quantitative assessment of skin layers absorption and skin reflectance spectra simulation in the visible and near-infrared spectral regions.* Physiological Measurement, 2002. **23**(4): p. 741-753.
118. Durr, N.J., *Nonlinear imaging with endogenous fluorescent contrast and plasmonic contrast agents*, in *The University of Texas at Austin*. 2010.
119. Lundgren, A., et al., *Method for preparing a surface with a controlled coverage of nanograde particles*. 2013, Google Patents.
120. Lundgren, A., et al., *Gold-Nanoparticle-Assisted Self-Assembly of Chemical Gradients with Tunable Sub-50 nm Molecular Domains.* Particle & Particle Systems Characterization, 2014. **31**(2): p. 209-218.
121. Elwing, H., et al., *A Wettability Gradient Method for Studies of Macromolecular Interactions at the Liquid/Solid Interface.* Journal of Colloid and Interface Science, 1987. **119**(1): p. 8.
122. Aili, D., et al., *Folding Induced Assembly of Polypeptide Decorated Gold Nanoparticles.* Journal of the American Chemical Society, 2008. **130**(17): p. 5780-5788.
123. Aili, D., et al., *Aggregation-Induced Folding of a De Novo Designed Polypeptide Immobilized on Gold Nanoparticles.* Journal of the American Chemical Society, 2006. **128**(7): p. 2194-2195.
124. Mak, W.C., et al., *Probing Zinc–Protein–Chelant Interactions Using Gold Nanoparticles Functionalized with Zinc-Responsive Polypeptides.* Particle & Particle Systems Characterization, 2014. **31**(11): p. 1127-1133.
125. Aili, D., et al., *Hybrid Nanoparticle−Liposome Detection of Phospholipase Activity.* Nano Letters, 2011. **11**(4): p. 1401-1405.
126. Zheng, K., et al., *Ultrafast laser parallel microdrilling using multiple annular beams generated by a spatial light modulator.* Journal of Physics D: Applied Physics, 2014. **47**(11): p. 115501.

127. Auksorius, E., et al., *Stimulated emission depletion microscopy with a supercontinuum source and fluorescence lifetime imaging.* Optics Letters, 2008. **33**(2): p. 113-115.
128. Becker, W., *The Bh TCSPC Handbook: Time-correlated Single Photon Counting Modules SPC-130, SPC-134, SPC-130 EM, SPC-134 EM, SPC-140, SPC-144, SPC-150, SPC-154, SPC-630, SPC-730, SPC-830 ; Simple-Tau Systems, SPCM Software, SPCImage Data Analysis*. 2012: Becker et Hickl.
129. Bashkatov, A.N., et al., *Optical properties of human skin, subcutaneous and mucous tissues in the wavelength range from 400 to 2000 nm.* Journal of Physics D: Applied Physics, 2005. **38**(15): p. 2543-2555.
130. Salomatina, E., et al., *Optical properties of normal and cancerous human skin in the visible and near-infrared spectral range.* Journal of Biomedical Optics, 2006. **11**(6): p. 064026-064026-9.
131. Eckardt, H., L. Fritsche, and J. Noffke, *Self-consistent relativistic band structure of the noble metals.* Journal of Physics F: Metal Physics, 1984. **14**(1): p. 97-112.
132. Borglin, J., et al., *Insights on proximity effect and multiphoton induced luminescence from gold nanospheres in far field optical microscopy.* Applied Physics Letters, 2015. **107**(23): p. 234101.
133. Zhu, D., et al., *Recent progress in tissue optical clearing.* Laser & Photonics Reviews, 2013. **7**(5): p. 732-757.
134. Horton, N.G., et al., *In vivo three-photon microscopy of subcortical structures within an intact mouse brain.* Nat Photon, 2013. **7**(3): p. 205-209.

Appendix A

3.1.1 The geometrical approach

```
%close all
clear all
clc
global w P0 b


att=15000; %scattering
pf=2;NA = 0.8;n = 1.33;a0 = 0.002;std=0.0015;P0 = 1; %set parameters
z = 0.0001:0.00005:0.0025;alpha = asin(NA/n);
%create grid and Gaussian collection window
[X,Y] = meshgrid(-pf*a0:0.00001:pf*a0, -pf*a0:0.00001:pf*a0);
[THETA,R] = cart2pol(X,Y);
gauss=exp( (-X.^2-Y.^2)/std^2 );

w0=[0.0019 0.0017 0.0015 0.0012 0.0010 0.0009];%compensated beamwaists
rat=[0 0.2 0.4 0.6 0.8 0.95];%ratios
b_vec = rat.*w0; %inner diameters

Mgauss=zeros(size(R,1),size(R,2),length(z),length(b_vec));%initialize
Mann=zeros(size(R,1),size(R,2),length(z),length(b_vec));

end_plot=length(z);%15;
find(gauss((size(gauss,1)-1)/2,:)>...
    (max(gauss((size(gauss,1)-1)/2,:))/2),1,'first')%FWHM of Gauss surface

Int_tot=zeros(length(b_vec),length(z),2);%initialize
Int_tot_sq=zeros(length(b_vec),length(z),2);
Int_tot_G=zeros(length(b_vec),length(z),2);
Int_tot_G_e=zeros(length(b_vec),length(z),2);
h = waitbar(0,'Progress');

for b_counter=1:length(b_vec)%for every inner radius
    waitbar(0,h,[num2str(b_counter),'/6 done']);
    b = b_vec(b_counter); %set parameters
    w=w0(b_counter);

    Ig = Igauss(R,THETA);%calculate surfaces
    Id = Idonut(R,THETA);
    Id(R<b) = 0;
    %Find FWHM
    find(Id((size(Id,1)-1)/2,:)>(max(Id((size(Id,1)-1)/2,:))/2),1,'first')
    wv = w*(1-z*tan(alpha)/a0); %parameters that depend on z
    bv = b*(1-z*tan(alpha)/a0);

    for j=1:length(z) %step into the sample
        waitbar(j/length(z),h)
        w = wv(j); %set parameters again
        b = bv(j);
        Ig = Igauss(R,THETA); %calculate the intensity
        Id = Idonut(R,THETA);
        Id(R<b) = 0;

        Mgauss(:,:,j,b_counter)=Ig; %store for offline analysis
        Mann(:,:,j,b_counter)=Id;
        %sum and calculate signals
        Int_tot(b_counter,j,:)=[sum(Ig(:)) sum(Id(:))];
```

```
        Int_tot_sq(b_counter,j,:)=[sum(Ig(:).^2) sum(Id(:).^2)];
        Int_tot_G(b_counter,j,:)=[sum(sum((Ig.^2).*gauss)) ...
            sum(sum((Id.^2).*gauss))];
        Int_tot_G_e(b_counter,j,:)=[Int_tot_G(b_counter,j,1).*...
            exp(-2*z(j)*att) Int_tot_G(b_counter,j,2).*exp(-2*z(j)*att)];
    end

end
close(h)

c_vec=['b' 'r' 'g' 'k' 'c' 'm'];%color vector

figure%plot the results
subplot(1,4,1)
hold on
plot(Int_tot_G_e(1,1:end_plot,1))
title('sum Int w Gauss and exp')
for i = 2:6
    plot(Int_tot_G_e(i,1:end_plot,2),c_vec(i))
end

subplot(1,4,2)
hold on
plot(log10(Int_tot_G_e(1,1:end_plot,1)))
title('log sum Int w Gauss and exp')
for i = 2:6
    plot(log10(Int_tot_G_e(i,1:end_plot,2)),c_vec(i))
end
subplot(1,4,3)
bar_data=sum(Int_tot_G_e(:,1:end_plot,2),2);
bar_data(1,:)=sum(Int_tot_G_e(1,1:end_plot,1),2);

bar(bar_data)
title('sum of OOF')
ylim([0 max(bar_data(:))])

subplot(1,4,4)
surf(gauss)
shading interp
title([num2str(std),' ',num2str(att),' ',num2str(end_plot)])
shg

figure %make a nice graph

bar(rat,bar_data)
colormap hot
xlim([-0.2 1.2])
set(gca,'XTickLabel','')
set(gca,'YTickLabel','')


function y = Idonut(r0,theta0)
global w P0 b
y = P0/(pi*w^2).*(1-b./r0).*exp(-2.*((r0-b)/w).^2);

function y = Igauss(r0,theta0)
global w P0
y = P0/(pi*w^2).*exp(-2.*(r0/w).^2);
```

```
%close all
clear variables
currentTimeAndDate = now;
currentDate = datestr(currentTimeAndDate);
currentDate=strrep(currentDate,' ','');
currentDate=strrep(currentDate,':','')%Savethedate

global r z w k F b

w0=[0.0019 0.0017 0.0015 0.0012 0.0010 0.0009]; %compensated beam waists

a = 0.002;n=1.33;

size_r=6; %um
size_z=6;
reso_r=300;
reso_z=300;%points
r_vec1=linspace(-size_r/1E6,size_r/1E6,reso_r*2+1);
r_vec2=0;%linspace(-size_r/1E6,size_r/1E6,reso_r*2+1);
k = 2*pi/800E-9; %Propagation number

[X,Y] = meshgrid(r_vec1,r_vec2);
[THETA,R] = cart2pol(X,Y);
result_matrix=zeros(4,size(R,1),size(R,2),reso_z);

bf=0;
bfVec=[0 0.2 0.4 0.6 0.8 0.95]; %ratios to test

%bfVec=0;
h=waitbar(0,'initializing...');
fname=['runstart',num2str(currentDate),...
    'data_block',num2str(currentDate),'.mat'];%for saving
%% for every inner radius blocked
for bfrac=bfVec
    bf=bf+1;
    for NA = 0.8
        w=w0(bf);
        F=a/(tan(asin(NA/n)));
        z_vec=linspace(-size_z/1E6,size_z/1E6,reso_z*2+1);

        zi=z_vec+F*ones(1,length(z_vec));
        b=a*bfrac;
        tic
        timet=0;
        ttotal=length(zi);

        for z=zi

            timet=timet+1;

            waitbar(0,h,[num2str(bf),'/',num2str(length(bfVec)),...
                ' ',num2str(timet),'/',num2str(ttotal)])
            E0 =  1;
            y = zeros(1,length(r_vec1));
            sub_t=0;
            sub_tt=size(R,1)*size(R,2)/4;
            %h2=waitbar(0,num2str(z));
            for j = 1:(size(R,1)+1)/2 %calculate on grid
                for ke = 1:(size(R,2)+1)/2
```

```
                    sub_t=sub_t+1;
                    waitbar(sub_t/sub_tt,h)

                    r = R(j,ke);
                    Psi = E0*k/z*quadgk(@fun3_160204, b, a);
                    y(ke) = abs(Psi^2);

                    result_matrix(bf,j,ke,timet)=y(ke);
                end
            end

            mirrortry=result_matrix(bf,1:(size(R,1)+1)/2,1:...
                (size(R,2)+1)/2,timet);
            result_matrix(bf,(size(R,1)+1)/2:end,1:...
                (size(R,2)+1)/2,timet)=flipud(squeeze(mirrortry));
            result_matrix(bf,:,(size(R,2)+1)/2:end,timet)...
                =fliplr(squeeze(result_matrix(bf,:,1:...
                (size(R,2)+1)/2,timet)));

        end
        toc

    end
end
close(h)
save(fname,'result_matrix')

function Y = fun3_160204(r0)
global r z w k F b

xvec = k*r0*r/z;

y1 = sqrt(1-b./r0).*exp(((r0-b)/w).^2);
y2 = exp(1i*k*(r0.^2/2/F-z-(r0.^2+r^2)/2/z));

Y=zeros(1,length(xvec));
for j = 1:length(xvec)
    x=xvec(j);
    y = besselj(0,x);
    y = 1/2/pi *y;
    Y(j) = y;
end
y3 = Y;
Y = y1.*y2.*y3;
```